Physics – Uspekhi **54** (11) 1091 – 1116 (2011)

REVIEWS OF TOPICAL PROBLEMS

PACS numbers: 61.72.Cc, 61.82.Rx, 62.20.fq, **62.25.–g**

Strength and plasticity of nanocrystalline materials and nanosized crystals

G A Malygin

DOI: 10.3367/UFNe.0181.201111a.1129

Contents

Abstract. The effect of grain boundaries and the crystal surface on the deformation and strength properties of nanocrystalline and nanosized materials, primarily metals, is reviewed. Basic experimental facts about the mechanical behavior of nanocrystal materials are presented and the observed findings are theoretically analyzed using equations of dislocation kinetics that take the properties of grain boundaries into account as sources, sinks, and dislocation barriers. Using a similar approach, size effects in the plastic deformation of micro- and nanocrystals are discussed by considering the crystal surface as a primary source of and sink for dislocations.

1. Introduction

Presently, the concept of a *nanostructure* involves a wide range of problems, including *nanocrystalline* (NC) materials and elements on the *nanometer* scale in various systems and devices. The common factor in all cases is the existence in the material or in the device of structural units less than 100 nm in size. In practice, however, materials and devices consisting of structural elements less than 1 μm in size frequently fall under the term nanostructure. The increased interest in the materials and structures of this type is explained by two related circumstances: their high strength and high functional properties, and the tendency to miniaturization of various systems and devices of electromechanics, robotics, electronics, medicine, and so on. As promising structural materials, nanocrystalline and microcrystalline metals and alloys have a sufficiently wide application already at present.

It so happened historically that the attention of researchers and technologists was primarily focused on micro- and nanocrystalline (metallic and ceramic) materials. They have high strength at low temperatures because of the Hall–Petch (HP) effect of grain-boundary strengthening [1] ($\sigma \sim d^{-1/2}$, where σ is the stress and d is the grain size) and exhibit unique technological properties (superplasticity [1, 2]) at increased temperatures because of the grain-boundary softening. The violation of the HP relation in nanomaterials at conventional (room) temperatures is also ascribed to the grain-boundary softening [3–6].

To date, a number of efficient methods of producing metallic materials with an ultrafine (10–1000 nm) grain have been developed, such as melt atomization or grinding a material in a ball mill with subsequent compacting of the produced nano- or micropowder into a polycrystalline aggregate. A widespread technique for producing micro- and nanocrystalline metallic films 0.1–10 μm thick is also a method for the deposition of atoms from the gas phase onto a substrate or deposition from an electrolytic solution.

The above methods mean the assembling (aggregation, consolidation) of a nanomaterial from separate structural elements such as atoms or nanoparticles. Another group of methods for producing NC materials is based on the processes of transformation of an initially coarse-crystalline or single-crystal metal or amorphous alloy (metallic glass) into an NC aggregate as a result of its severe plastic deformation by methods such as equal-channel angular pressing (ECAP) [7], rolling [8], or high-pressure torsion (HPT) [9]. In the case of amorphous alloys, their nanocrystallization can be achieved, apart from severe deformation [10, 11], by using traditional methods, e.g., by heating them to the crystallization temperature [12].

Along with nanocrystalline materials, much attention has also been paid in the last few years to the investigation of the strength and deformation properties of single-crystal samples

---

G A Malygin Ioffe Physicotechnical Institute,
Russian Academy of Sciences,
ul. Politekhnicheskaya 26, 194021 St. Petersburg, Russian Federation
E-mail: malygin.ga@mail.ioffe.ru

Received 3 March 2011, revised 15 April 2011
Uspekhi Fizicheskikh Nauk **181** (11) 1129 – 1156 (2011)
DOI: 10.3367/UFNr.0181.201111a.1129
Translated by S N Gorin; edited by A M Semikhatov

of pure metals and alloys whose transverse size in one or two directions is less than 1 micron. Tensile tests of samples of fcc and bcc metals in the form of filamentary crystals (whiskers) 5–20 μm in diameter, which were performed in the 1950s [13–15], showed that these crystals have a high strength and can be elastically deformed to 2%.

An important achievement of recent years is the development of methods of production and investigation of the mechanical properties of single-crystal samples with transverse dimensions in the submicron and nanometer ranges. In [16, 17], the etching of the surface of a metallic single crystal by a focused ion beam was used for this purpose; as a result, samples in the form of micropillars were formed on the surface, which had a diameter of 100–1000 nm and a height of several microns. These micropillars were subjected to compressive deformation using a diamond nanoindenter with a flattened tip. A further development of this method is the etching of the surface of a two-phase alloy using a focused ion beam with the purpose of forming a 'forest' of micropillars of one of the two phases on the surface, with the subsequent deformation of these pillars using a nanoindenter [18]. In [19], the NEMS technology (nanolithographic etching of thin metallic films deposited on a substrate) was applied to fabricate polycrystalline samples 300–500 nm thick. This technology allows preparing not only specimens for tensile and bending tests, but also loading and measuring devices for their investigation in a single film construction.

The investigation of the mechanical properties of crystals with transverse dimensions in the submicron and nanometer range [16, 17] showed that their strength approaches theoretical values in accordance with the law $\sigma \sim D^{-n}$, where D is the transverse size of the crystal and $n \approx 0.6-1.0$.

One more size effect that has attracted the attention of researchers in the last decade is the enhanced strength of metallic samples (wires) 1–10 μm in diameter subjected to torsion, in comparison with their strength under homogeneous tensile deformation [20]. A similar effect was revealed in the plastic bending of thin metallic films of micron thickness [21, 22] and in the micro- and nanoindentation of materials [23–25], i.e., the processes that also occur under plastic deformation, which is inhomogeneous on the microscale. The enhanced strength of ultrathin samples in these cases is ascribed to the generation in them of additional (compared to uniform deformation) *geometrically necessary* (GN) dislocations because of the existence of large gradients of plastic deformation under a torsion or bending deformation inhomogeneous on the microlevel [20–22].

In the foregoing, we described traditional materials (metals and alloys) in which the predominant mechanism of plastic deformation is the dislocation mechanism. But in the last three decades, numerous investigations have been devoted to the unusual properties of alloys with a shape-memory effect (SME), which undergo martensitic reversible structural phase transformations [26–30]. Their characteristic feature is a superlarge (compared to the traditional piezo crystals and magnetostrictive materials) SME deformation (5–15%) sensitive to temperature and mechanical stresses and magnetic fields [29–30]. The above facts serve as a basis for numerous applications of these alloys (e.g., TiNi) in medicine, astronautics, and energy engineering for use as force actuators, sensors, and functional (smart) elements of various systems and devices, e.g., micro- and nanoelectromechanical systems (MEMS and NEMS) [31]. The last circumstance served as a stimulus for studying the influence of the size effect on both the parameters of martensitic transitions in such alloys [32–35] and their operational characteristics (force and deformation) [36–38]. The results of work performed to date have shown a high sensitivity of the above parameters and characteristics to this factor.

The above brief review of experimental investigations of the influence of the grain size in polycrystals and of the single-crystal structure on the strength and functional properties of a large group of materials that are promising for applications indicates the importance and the fundamental character of this avenue of investigation. The results of these investigations concerning the strength properties of NC materials have been summarized in a number of recent reviews [39–43]. The results of the first stage of the investigation of strength and deformation properties of single-crystal nanosized samples of pure metals and alloys are contained in review papers [44, 45]. The effect of gradients of plastic deformation and of GN dislocations on the deformation and strength properties of samples of thin (micron thickness) sections has been considered in a special issue of *Scripta Materialia* [46] and in review [22]. The problem of the influence of the size factor on the parameters of martensitic transitions in SME alloys and on the functional properties of these alloys is now at the initial stage. In this review, we therefore restrict ourselves to references to the main experimental [26–38] and theoretical [65–71] investigations of this issue available to date.

In spite of a large number of studies concerning the investigation of the effect of the size factor on the strength and deformation properties of crystalline materials performed to date, the physical mechanisms of this influence are currently debatable [39–43]. Three systematic theoretical approaches to the investigation of these questions exist now. The first two are based on the methods of computer simulation; these are the molecular-dynamics (MD) method [47–50] and the method of 3D dynamics of discrete dislocations (3D-DDD) [51–55]. The third method is based on the dislocation-kinetics equations [4, 40, 56–58], which describe the evolution of the density of dislocations in nanomaterials taking the structural features of grain boundaries and of the surface of micro- and nanocrystals into account as sources of, sinks for, and barriers to dislocations. One more theoretically consistent method is that of an analysis of the energy stability of dislocation micro- and nanostructures [59–62], which is based on the continuum theory of dislocations and disclinations.

These methods are microscopic, i.e., they consider phenomena starting at the elementary (molecular or dislocation) level and then pass to the meso and macro levels. The model (heuristic) method based on phenomenological relations [5, 63, 64] has not yet exhausted its potential, either. Each of the above methods has its own advantages and disadvantages, and should therefore be considered as complementing one another.

The MD simulation [65] and the dislocation-kinetics approach [29] are also used in the analysis of the mechanisms underlying the effect of the size factor on martensitic transitions and on the deformation behavior of SME alloys. The dislocation-kinetics method allows describing the effect of structural factors, including the size factor, on the kinetics and thermodynamics of martensitic transformations in SME alloys [34, 38, 66]. Dislocations are here understood as dislocations of the lattice [67] and twin [68] transformation types and steps (ledges) of nanometer height at interphase boundaries [29, 69]. From the thermodynamic phenomenological standpoint, the effect of the grain size on the critical temperature of a martensitic transformation was discussed in [70, 71].

This review is aimed at a theoretical analysis of the data available in the literature on the strength and plasticity of nanocrystalline materials predominantly in terms of the dislocation-kinetics approach. This issue is considered in Section 2. In Section 3, an analogous approach is used to consider the effect of the size factor on the strength of crystals and samples with transverse dimensions in the micro- and nanorange. Section 4 is devoted to a discussion of the results of the analysis and conclusions.

2. Nanocrystalline materials

From the dislocation-kinetics standpoint, the effect of the size factor on the strength and plasticity of micro- and nanocrystalline materials was discussed in recent review [40]. However, the rate of investigations of this question is presently so high that a variety of new data have appeared that require new understanding in terms of this approach. In Section 2.1, we consider data indicating that up to the crystallite size of 2–3 nm [72], it is precisely the dislocation mechanism that determines the strength and plastic properties of nanometals and the features of their deformation, such as the dependence of the coefficient of the strain-rate sensitivity of plastic flow [73–79] and activation volumes [42, 76, 77, 80] on the size of crystallites, and the formation of shear microbands [81–84]. In Section 2.2, we discuss methods of improving plastic properties of nanometals without a noticeable reduction in their strength, namely, the creation of bimodal micronanograined [85–91] and nanotwinned submicrograined [92–101] structures.

2.1 Dislocation mechanism of nanostrength and nanoplasticity

2.1.1 Hall–Petch relation. Three issues remain debatable regarding the problem of plasticity and strength of NC metals: (1) the character of the breakdown of the Hall–Petch (HP) relation in the case of grains less than 10–20 nm in size, (2) the mechanism of this breakdown, and (3) the role of dislocations in this mechanism. For example, Fig. 1a displays the experimental data on the microhardness H of a nanocrystalline Ni–W alloy [72], which indicate that at crystallite sizes less than 7–10 nm, the HP law $H \sim d^{-1/2}$ for the microhardness is violated and a tendency appears toward the formation of the inverse HP relation, $H \sim d^{p}$, with an exponent $p > 0$. Positive values $p = 0.2-0.5$ at the nanograin sizes $d < 10-15$ nm were also observed in a number of other NC materials [3–6, 40–43, 47–49, 73–70, 88]. These values indicate a crossover from the mechanism of grain-boundary strengthening of a nanomaterial to a mechanism of grain-boundary softening.

As regards the Ni–W alloy, it was found in [80] that its microhardness at the grain size less than 15 nm deviates from the HP relation, but remains approximately constant, independent of the grain size down to $d = 3$ nm (Fig. 1b). Just as in the above-considered case (Fig. 1a), the NC samples were obtained by the method of electrodeposition. It can be seen from Fig. 1a that at $d < 10$ nm, a spread of experimental points is observed, which hampers the detection of a clear tendency of the variation of H in this range of grain sizes. This fact and other similar circumstances frequently serve as grounds for the conclusion [39] that the violation of the HP relation for the grain sizes less than 10 nm is not related to grain-boundary softening, but can be ascribed to a gradual filling of the nanograin volume by a 'mantle' of dislocations emitted by grain boundaries, after which the microhardness of the nanomaterials stops being dependent on the size of the nanograins. The authors of [80], whose results are shown in Fig. 1b, ascribe the deviation from the HP relation to the amorphization of the nanomaterial structure. As one more argument in favor of this statement, they indicate the local instability of the process of plastic deformation of the nanoalloy, namely, the formation in it of shear microbands similar to plastic-flow bands in amorphous metallic alloys.

It is obvious that the above contradictory observations and the conclusions following from them require a more detailed discussion, covering additional experimental and theoretical methods for the analysis of the data available in the literature. The results obtained in this area are discussed in

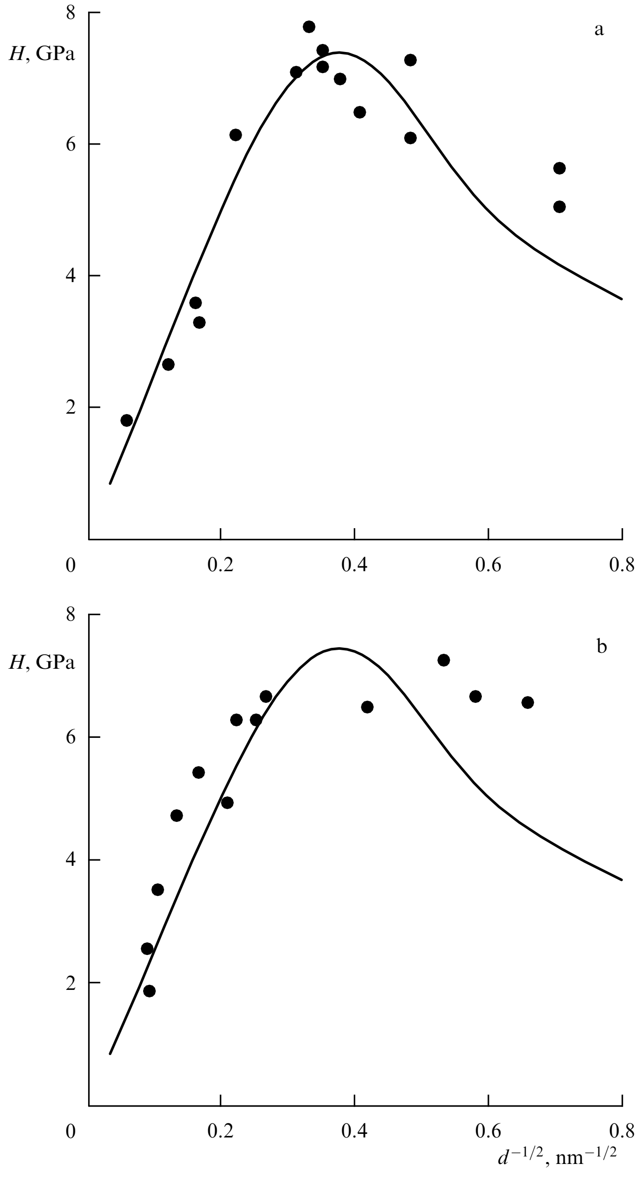

Figure 1. Microhardness H of the nanocrystalline Ni–W alloy as a function of the grain size d: (a) data in [72]; (b) data in [80]. The curves are constructed in accordance with Eqn (4).

Sections 2.1.2–2.1.4.

2.1.2 Dislocation-kinetics analysis of flow stresses in nanocrystalline metals.

The curves in Figs 1a and 1b have been constructed based on the assumption that at grain sizes less than 10 nm, the grain-boundary softening related to annihilation of dislocations in the boundaries of nanograins occurs. The calculation of these curves is based on the kinetic equation for the average dislocation density ρ in the nanomaterials and for its evolution with respect to the shear deformation γ [4, 40, 79]:

$$\frac{\mathrm{d}\rho}{\mathrm{d}\gamma} = \frac{\beta}{bd} - (k_\mathrm{a} + k_\mathrm{b})\,\rho,$$
$$k_\mathrm{b} = 4\eta_\mathrm{b}\,\frac{D_\mathrm{gb}}{m_\mathrm{T}\dot{\varepsilon}d^2} = \left(\frac{d_\mathrm{b}}{d}\right)^2, \quad d_\mathrm{b} = \left(\frac{4\eta_\mathrm{b}D_\mathrm{gb}}{m_\mathrm{T}\dot{\varepsilon}}\right)^{1/2}. \tag{1}$$

Here, $d_\mathrm{b} = d_\mathrm{b}(T, \dot{\varepsilon})$ is the characteristic size of nanograins corresponding to the onset of grain-boundary softening, β is the coefficient that determines the rate of accumulation of dislocations in the bulk of grains because of the restriction of the free path of dislocations to the grain size ($\beta \approx 1$), b is the Burgers vector, k_a is the coefficient of annihilation of screw dislocations via the cross slip mechanism, k_b is the coefficient of annihilation of edge dislocations accumulated in the boundaries and near the nanograin boundaries, $D_\mathrm{gb} = D_\mathrm{gb}(T)$ is the grain-boundary diffusion coefficient, T is the temperature, $\eta_\mathrm{b} \approx \mu b^3/k_\mathrm{B}T$, k_B is the Boltzmann constant, $\dot{\varepsilon} = \dot{\gamma}/m_\mathrm{T}$ and $\dot{\gamma}$ are the respective rates of uniaxial and shear deformation, $m_\mathrm{T} = 3.05$ is the Taylor orientation factor, and μ is the shear modulus. The right-hand side of Eqn (1) does not contain the term $k_\mathrm{f}\rho^{1/2}$ characteristic of coarse-grained ($d > 1-10$ μm) materials, which describes the dislocation multiplication on forest dislocations, because the characteristic spacing between the events of multiplication of dislocations on forest dislocations ($\lambda_\mathrm{f} = 1/\delta_\mathrm{f}\rho^{1/2}$, where $\delta_\mathrm{f} = bk_\mathrm{f} \approx 10^{-2}$) is substantially greater than the size of nanograins [40]. For example, at $\rho = 10^{14} - 10^{16}$ m^{-2}, this spacing is 1–10 μm.

Integrating Eqn (1), we find the dependence of the dislocation density in the nanomaterials on the uniaxial deformation degree $\varepsilon = \gamma/m_\mathrm{T}$:

$$\rho(\varepsilon) = \rho_0 \exp(-m_\mathrm{T}k\varepsilon) + \rho_\mathrm{m}\left[1 - \exp(-m_\mathrm{T}k\varepsilon)\right], \tag{2}$$

where $\rho_0 = \beta_0/bd$ is the initial ($\varepsilon = 0$) dislocation density due to their generation from grain boundaries [40, 192], β_0 is a coefficient depending on the density of ledges in the grain boundaries, $k = k_\mathrm{a} + k_\mathrm{b}$, and $\rho_\mathrm{m} = \beta/bdk$ is the equilibrium dislocation density for $\varepsilon \to \infty$. With Eqn (2) and the Taylor relation $\tau = \alpha\mu b\rho^{1/2}$, the dependence of the flow stress $\sigma = m_\mathrm{T}\tau$ of an NC material on the deformation ε is given by

$$\sigma(\varepsilon) = m_\mathrm{T}\alpha\mu b\Big\{\rho_0 \exp(-m_\mathrm{T}k\varepsilon) + \rho_\mathrm{m}\left[1 - \exp(-m_\mathrm{T}k\varepsilon)\right]\Big\}^{1/2}, \tag{3}$$

where α is the dislocation interaction constant. Because $\rho_0 \sim \rho_\mathrm{m} \sim d^{-1}$, Eqn (3) can be written as

$$\sigma(\varepsilon) = m_\mathrm{T}\alpha\mu\left(\frac{b}{d}\right)^{1/2}\bigg\{\beta_0 \exp(-m_\mathrm{T}k\varepsilon) + \frac{\beta}{k}\left[1 - \exp(-m_\mathrm{T}k\varepsilon)\right]\bigg\}^{1/2}. \tag{4}$$

The results of electron-microscopic investigations [103, 104] and computer simulations [47–49, 105] of the processes of plastic deformation of NC metals show that the grain boundaries are (1) sources of dislocations, (2) barriers that favor the accumulation of dislocations inside the nanograins, and (3) sinks for dislocations. It is precisely these kinetic processes that are taken into account in Eqns (1) and (2) for the density of dislocations and Eqns (3) and (4) for the flow stress. The parameters β_0 and β determine the rate of the first two kinetic processes; the coefficient of annihilation of dislocations $k = k_\mathrm{a} + k_\mathrm{b}(d, T, \dot{\varepsilon})$, which depends on the grain size d, the temperature T, and the strain rate ε [Eqn (1)], controls the efficiency of grain boundaries as sinks for lattice dislocations.

In Figures 1a and 1b, the theoretical curves are constructed using Eqn (4) under the assumption that $H = 3\sigma_\mathrm{y}$, where $\sigma_\mathrm{y} = \sigma(\varepsilon_\mathrm{y})$ is the yield stress, $\varepsilon_\mathrm{y} = 0.2\,\%$, $d_\mathrm{b} = 80$ nm, and $\beta_0 = 6 \times 10^{-3}$ (the values of the other parameters are given in [79]). At $k_\mathrm{a} = 0$ and $m_\mathrm{T}k_\mathrm{b}\varepsilon_\mathrm{y} \ll 1$, i.e., at grain-boundary sizes $d \gg (m_\mathrm{T}\varepsilon_\mathrm{y})^{1/2}d_\mathrm{b} \approx 14$ nm, Eqn (4) yields the normal HP relation $H = K_\mathrm{HP}d^{-1/2}$, which describes the effect of grain-boundary strengthening of a polycrystalline material (here, $K_\mathrm{HP} = 3m_\mathrm{T}\alpha\mu b^{1/2}(\beta_0 + m_\mathrm{T}\beta\varepsilon_\mathrm{y})^{1/2}$ is the HP coefficient for the microhardness). In the other extreme case $m_\mathrm{T}k_\mathrm{b}\varepsilon_\mathrm{y} \gg 1$, i.e., at sufficiently small grain sizes and relatively large deformations, we obtain the inverse HP relation $H = K'_\mathrm{HP}d^{1/2}$, where $K'_\mathrm{HP} = 3m_\mathrm{T}\alpha\mu(\beta b/d_\mathrm{b}^2)^{1/2}$ describes the phenomenon of grain-boundary softening of a nanomaterial. It can be seen from Figure 1a that within the spread of experimental data, Eqn (4) agrees sufficiently well with the experimental data in the regions of normal and inverse HP relations down to the grain size 2–3 nm. An agreement of Eqn (4) with the data on the microhardness and yield stress is also observed for other NC metals [40, 79].

The situation is different in Figure 1b, where in the region of grain sizes $d < 15$ nm, the experimental points deviate strongly from the theoretical curve. To resolve this contradiction, it is necessary to resort to additional data (see Sections 2.1.3 and 2.1.4) in order to clarify to which extent the results given in Figure 1b at the grain sizes less than 15 nm are universal.

2.1.3 Coefficient of the strain-rate sensitivity of the flow stresses.

A traditional method of studying physical mechanisms of deformation of crystalline materials, depending on the material structure, is the thermoactivation analysis of their plastic and strength properties. Important indicators here are the data on the strain-rate and temperature dependences of the flow stress $\sigma = m_\mathrm{T}\tau$, such as the coefficient of strain-rate sensitivity (SRS) of the flow stress $m = \mathrm{d}\ln\sigma/\mathrm{d}\ln\dot{\varepsilon} = k_\mathrm{B}T/V\tau$ and the activation volume V. Figure 2a displays the results of the determination of the coefficient m for the microhardness H (of the yield stress $\sigma_\mathrm{y} = H/3$) of polycrystalline copper depending on the grain size in a wide range, from 10 to 10^6 nm [77]. It can be seen that for the grain sizes $d < 1$ μm, the coefficient m in NC copper is much higher than that for coarse-grained copper (dashed line). Figure 2b demonstrates the variation of the activation volume V (expressed in b^3 units) in a number of fcc NC metals (Ni [76], Cu [77], Ni–W alloy [80]) depending on grain refinement. It can be seen that the activation volume decreases substantially with decreasing the grain size.

The activation volume depends on the spacing l between the obstacles characterized by a short-range radius, which are

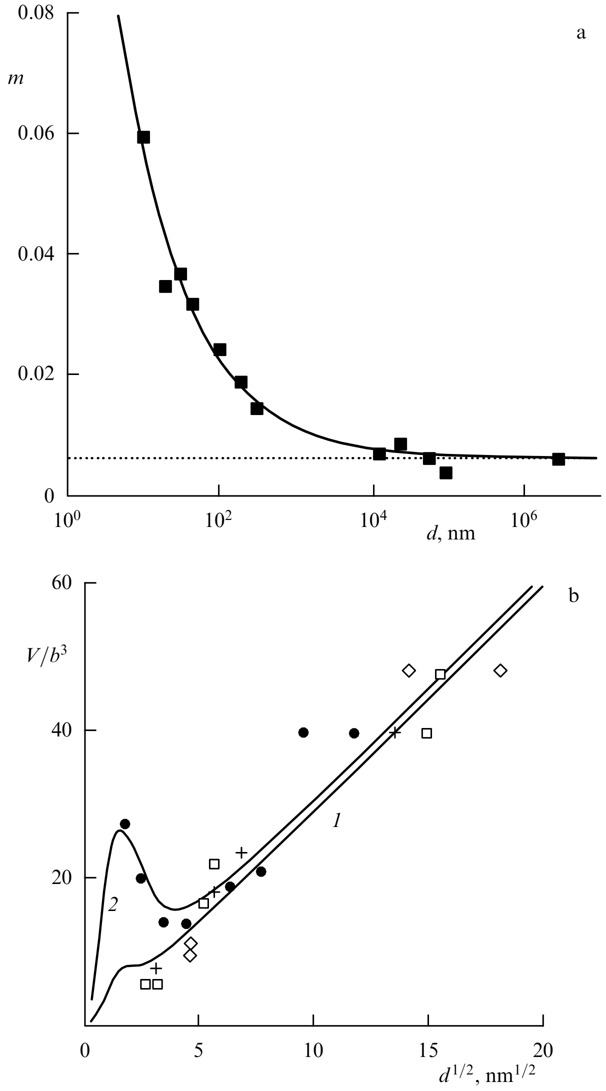

Figure 2. Dependences of (a) the coefficient of strain-rate sensitivity m of NC copper on the grain size d [77] [the curve was constructed using Eqn (6a)] and (b) the activation volume V on the grain size in fcc NC metals: (□) Cu [80]; (◇) Ni [76]; (●) Ni–W alloy [80]; (+) Cu [77] [curves *1* and *2* are constructed according to Eqn (5b)].

overcome by dislocations as a result of thermofluctuations, and on the activation width of the obstacle $\Delta x = vb$: $V = b\Delta x l = vb^2 l$, where v is the obstacle width in Burgers-vector units. In the presence of obstacles of various types, the effective activation volume is $V^{-1} = V_1^{-1} + V_2^{-1}$, whence

$$V = \frac{b^2}{1/v_1 l_1 + 1/v_2 l_2} \,. \tag{5a}$$

The subscripts 1 and 2 mark the values of the corresponding parameters of the obstacles. In pure fcc metals, two types of obstacles exist in nanograins; these are, as follows from the results of MD simulations [48, 106], nanograin boundaries against which the ends of the dislocation loops rest during their motion in slip planes, and forest dislocations inside the grains in the case of multiple slip. In the case of obstacles in grain boundaries, the activation length is determined by the grain size: $l_1 = \xi_1 d$, where $\xi_1 < 1$ is a parameter that depends on the curvature of the loop and the shape of the grain. For forest dislocations in intersecting slip planes, the activation length is determined by the dislocation density: $l_2 = \xi_2/\rho^{1/2}$, where $\xi_2 \approx 1$. Substituting these relations in Eqn (5a), we obtain the dependence of the activation volume on the nanograin size and dislocation density,

$$V = \frac{\eta_1 b^2 d}{1 + (\eta_1/\eta_2)\, d\rho^{1/2}} \,, \tag{5b}$$

where $\eta_1 = v_1 \xi_1$ and $\eta_2 = v_2 \xi_2$.

In accordance with (5b), curves *1* and *2* in Figure 2b show the dependence of the activation volume on the grain size in the coordinates $(V/b^3,\ d^{1/2})$. In constructing curve *1*, the following values of the parameters of NC copper were used: $b = 0.25$ nm, $d_{\mathrm{b}} = 80$ nm, $\eta_1 = 1.7$, and $\eta_2 = 0.17$. At sufficiently large grain sizes ($d \gg (m\varepsilon_{\mathrm{y}})^{1/2} d_{\mathrm{b}} \approx 20$ nm), according to (2) and (3), we have the following relation for the dislocation density at the yield stress: $\rho_{\mathrm{y}} \approx (\beta_0 + m\beta\varepsilon_{\mathrm{y}})/bd$. After its substitution in Eqn (5b), we find, in agreement with the experiment in [42, 76, 77, 80], that

$$V \approx \frac{\eta_2 (d/b)^{1/2} b^3}{\left(\beta_0 + m_{\mathrm{T}}\beta\varepsilon_{\mathrm{y}}\right)^{1/2}} \sim d^{1/2} \,. \tag{5c}$$

In the other extreme case of small grain sizes, $\rho_{\mathrm{y}} \approx \beta/bd$, whence, in accordance with (5b), $V = \eta_1 b^2 d$. A segment of curve *1* for nanograins with $d < 7$ nm corresponds to the dependence $V \sim d$ in Fig. 2b, where the grain-boundary softening due to the annihilation of dislocations in grain boundaries occurs. It also follows from the data presented in Fig. 2b that in the case of the Ni–W alloy [80] at the grain size less than 15 nm, the activation volume increases as $V \sim d^{-1/2}$. Curve *2* in this figure demonstrates the results of calculations of the $V(d)$ dependence in accordance with (5b) at the parameter values $d_{\mathrm{b}} = 180$ nm, $\eta_1 = 8.5$, and $\eta_2 = 0.17$.

The analysis of the nanograin-size dependence of the activation volume in the Ni–W alloy therefore shows that at the smallest sizes, the plastic deformation of the alloy is controlled by dislocation motion, and the deviation of the experimental points in Fig. 1b from the theoretical curve is therefore not regular.

An important argument in favor of the dislocation mechanism of plastic deformation of nanograined materials is the existence of data on the grain-size dependence of the SRS coefficient m of the flow stress for the NC samples of metals with fcc (Fig. 2a) and bcc (Fig. 3) structures. In the case of sufficiently pure NC metals with an fcc structure, the only barriers to moving dislocations inside grains, as was noted above, are forest dislocations with the average spacing $l_2 = \xi_2/\rho^{1/2}$ between them. The activation volume V for them is determined by Eqn (5b). Substituting (5b) in the relation $m = k_{\mathrm{B}}T/V\tau$ for the SRS coefficient and using the relation $\tau = \alpha\mu b\rho^{1/2}$, we obtain the following dependence of m on d and ρ:

$$m = m_{\mathrm{d}}\left(1 + \frac{\eta_2}{\eta_1 d\rho^{1/2}}\right), \quad m_{\mathrm{d}} = \frac{k_{\mathrm{B}}T}{\alpha\eta_2\,\mu b^3} \,, \tag{6a}$$

where m_{d} is the SRS coefficient in a coarse-grained material. Taking into account that $\rho \approx \chi_{\mathrm{y}}/bd$ at the yield stress, where $\chi_{\mathrm{y}} = \beta_0 + m_{\mathrm{T}}\beta\varepsilon_{\mathrm{y}}$, we finally find

$$m = m_{\mathrm{d}}\left[1 + \frac{\eta_2}{\eta_1 \chi_{\mathrm{y}}}\left(\frac{b}{d}\right)^{1/2}\right] . \tag{6b}$$

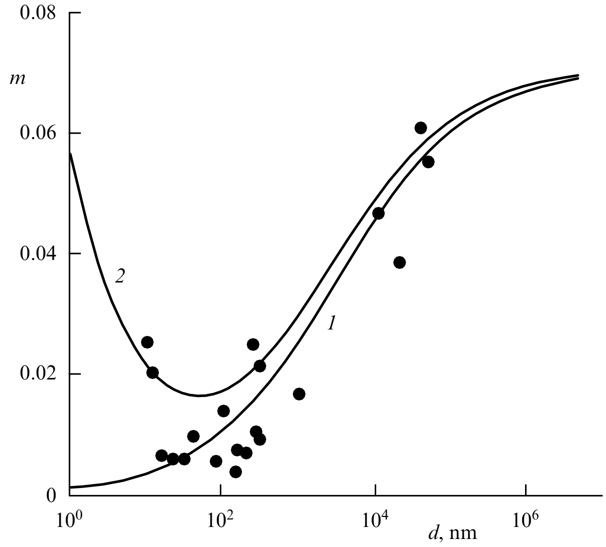

Figure 3. Dependence of the SRS coefficient m of the yield stress of α-Fe on the grain size d [74]. Curves *1* and *2* were constructed respectively using Eqns (8b) and (8c).

The curve in Fig. 2a demonstrates the $m(d)$ dependence in accordance with Eqn (6b) at $\eta_2/\eta_1\chi_y = 83$, $b = 0.26$ nm, and $m_d = 6.4 \times 10^{-3}$ [77, 79]. Relation (6b) can be written in a more compact form as

$$m = m_d \left[1 + \left(\frac{d_y}{d} \right)^{1/2} \right], \tag{6c}$$

where $d_y = (\eta_2/\eta_1\chi_y)^2 b \approx 2$ μm is the characteristic grain size at which this size starts affecting the SRS of the yield stress (microhardness) of the NC material.

It follows from the data in Fig. 3 that in bcc metals, in contrast to fcc metals, the grain refinement leads to a decrease in the SRS coefficient of the flow stress rather than to its increase. In bcc metals at temperatures below $0.15T_m$, an obstacle to dislocations inside the nanograins, along with forest dislocations, is given by a Peierls relief with the characteristic activation length l_P equal to the critical size of a double kink [106, 107]. Taking this into account, we have the following relation for the effective activation volume: $V^{-1} = V_1^{-1} + V_2^{-1} + V_3^{-1}$, where $V_3 = v_3 b^2 l_P$ and, consequently,

$$V = \frac{\eta_1 b^2 d}{1 + (\eta_1/\eta_2)\, d\rho^{1/2} + (\eta_1/v_3)(d/l_P)} \,. \tag{7}$$

Taking into account that the flow stress $\tau = \tau_P + \alpha\mu b\rho^{1/2}$ in this case includes the Peierls stress τ_P, we express the strain-rate coefficient as

$$m = m_P \frac{1 + (v_3/\eta_1)(l_P/d) + (v_3/\eta_2)\, l_P\rho^{1/2}}{1 + \alpha(\mu/\tau_P)\, b\rho^{1/2}} \,, \qquad m_P = \frac{k_B T}{v_3 b^2 l_P \tau_P} \,, \tag{8a}$$

where m_P is the strain-rate coefficient for the coarse-grained bcc metal. Curve *1* in Fig. 3 illustrates the $m(d)$ dependence given by Eqn (8a) with $\rho \approx \chi_y/bd$ and $d \gg l_P$. This relation can now be written in the compact form

$$m = m_P \left[1 + \left(\frac{d_P}{d} \right)^{1/2} \right]^{-1}, \quad d_P = \left(\frac{\alpha\mu}{\tau_P} \right)^2 \chi_y b \,, \tag{8b}$$

where d_P is the characteristic grain size at which it starts significantly affecting the SRS coefficient of the yield stress of the bcc metal. The curve in Fig. 3 corresponds to formula (8b) with $d_P = 2.9$ μ and $m_P = 0.07$.

It also follows from the data in Fig. 3 that at the size of nanograins $d < 10$ nm, the coefficient m tends to increase. This tendency can be caused by two circumstances [79]: (1) a grain size less than the size of the double kink l_P (in α-Fe, $l_P = 30b \approx 7.5$ nm [107]) and (2) the dislocation density $\rho \sim d$ that decreases as the size of nanograins decreases because of the annihilation of dislocations in their boundaries. Curve *2* in Fig. 3 illustrates the first circumstance in accordance with the relation

$$m = m_P \frac{1 + (v_3/\eta_1)(l_P/d)}{1 + (d_P/d)^{1/2}} \,, \tag{8c}$$

where $v_3/\eta_1 = 5$, $l_P = 7.5$ nm, and $d_P = 2.9$ μm. The second circumstance, i.e., the grain-boundary softening, has been discussed in [79].

The analysis of deviations from the HP relation and of the peculiarities related to the dependence of the activation volume V and the SRS coefficient m on the grain size, which has been performed in terms of the dislocation-kinetics approach, thus shows that the decisive role belongs to dislocations in all the above cases.

2.1.4 Shear microbands. As has been established in [81, 82], the plastic deformation of iron nanocrystalline samples occurs inhomogeneously, with the formation of shear microbands of the width $w \approx 60d$, with the average spacing between the bands $\Lambda \approx (2-10)\, w$, and with the magnitude of shear in the bands equal to 200–300%. Such an inhomogeneity of deformation is observed only if the grain size is less than a certain critical value d_c. In NC iron, the critical size is 300 nm [82]. An electron-microscopic investigation shows that inside microbands, nanograins are strongly elongated in the direction of maximum tangential stresses and contain a large density of dislocations, but remain undeformed between the bands. The character of plastic deformation that is inhomogeneous at the microlevel was also revealed in some other NC metals [83, 84].

It can be supposed that the formation of a regular system of microbands in this case, just as in some other cases of plastic deformation that is inhomogeneous on the microlevel [86], is related to the process of spatial self-organization of dislocations. A characteristic feature of plastic deformation of NC materials is, as was already said above, the predominant role of grain boundaries as sources of, barriers to, and sinks for dislocations. These features are taken into account by the kinetic equation for the density of dislocations [83]

$$\rho \frac{\partial \rho(x, y, \gamma)}{\partial \gamma} + (\xi - 1)\, \frac{\lambda_D}{b} \left(\frac{\partial^2 \rho}{\partial y^2} + \frac{M}{\rho} \left(\frac{\partial \rho}{\partial y} \right)^2 \right) = (1 - \beta_{gb})\, \frac{n}{b} + \frac{\beta}{bd}\, \rho - k_a \rho^2 \,, \tag{9}$$

where x is the coordinate in the direction of the elongation of microbands (in the direction of the action of maximum tangential stresses), y is the coordinate in the direction of the expansion of the bands, $\lambda_D \approx d$ is the length of the diffusion path of dislocations upon expansion of a microband, $\xi > 1$ is a parameter that ensures the spatial instability of the dislocation density distribution (Turing instability [108, 109]), $M = 1/m(d)$ is a coefficient that accounts for the dispersion of the dislocation velocity because of its dependence on the dislocation density, and $m(d)$ is, as before, the SRS coefficient of the flow stress. In Eqn (9), the first term in the right-hand side describes the balance of the densities of dislocation sources $n = (sl_{\rm b}d)^{-1}$ and sinks $n_{\rm g} = \beta_{\rm gb}n$ in grain boundaries, where $s \approx 2b$ is the width of boundaries, $l_{\rm b}^{-1}$ is the linear density of sources on the boundary, and the parameter $\beta_{\rm gb} = n_{\rm g}/n$ determines the relative efficiency of grain boundaries as sources of and sinks for dislocations. The second term reflects the process of dislocation accumulation inside nanograins due to the restriction of their free path to the grain size ($\beta \approx 1$), and the third term takes the annihilation of the screw components of dislocation loops into account.

Because the rate of elongation of microbands is substantially greater than the rate of their expansion, instead of a two-dimensional problem, we consider its one-dimensional analog, $\rho = \rho(y, \gamma)$. The solution of linear equations (9) can be sought in the form $\rho = v(\gamma)\,\psi(y)/bd$, with the equation

$$v(\gamma) = \beta_0 \exp(-k_{\rm a}\gamma) + \frac{\beta}{k_{\rm a}}\big(1 - \exp(-k_{\rm a}\gamma)\big) \qquad (10)$$

describing the deformation-related part of the evolution of the dislocation density in the NC metal [see Eqn (2)]. After the substitution of (10) in (9) and separation of the variables γ and y, we obtain an equation for the spatial part of the dislocation density $\psi(y)$:

$$\frac{\partial^2\psi}{\partial Y^2} + \frac{M}{\psi}\left(\frac{\partial\psi}{\partial Y}\right)^2 = (1 - \beta_{\rm gb})\,\frac{d}{v_0(\gamma)\,d_0} + \psi - \psi^2\,. \qquad (11)$$

Here, $Y = y/\Lambda_0$, $\Lambda_0(d) = \left[(\xi - 1)\,\lambda_{\rm D}d/\beta\right]^{1/2} \sim d$, and $d_0 = \beta^2 sl_{\rm b}/bk_{\rm a}$. The right-hand side of Eqn (11) contains the function $v_0(\gamma) = (k_{\rm a}/\beta)\,v(\gamma)$, which only slightly differs from unity at $\beta_0 \approx \beta/k_{\rm a}$; we can therefore assume that the variables y and γ actually separate in Eqns (10) and (11).

At $\beta_{\rm gb} > 1$ and the boundary condition $\mathrm{d}\psi/\mathrm{d}Y|_{\psi=0} = 0$, the solution of Eqn (11) is an elliptic integral of the first kind, $F(\theta, k)$ [83]. Using the Jacobi elliptic function $sn(y)$, this solution can be written in a compact form as

$$\psi(y, d) = \frac{\psi_0(d)}{1 - k^2 sn^2\big(y/\Lambda(d)\big)}\,, \qquad (12)$$

where $\psi_0(d)$ and $\Lambda(d)$ are the dimensionless dislocation density between the microbands and the spacing between them, and $k = k(d)$ is the modulus of the elliptic integral. Explicit dependences of these parameters on d are given in [83]. Figures 4a and 4b show the distribution of the density of dislocations in an NC metal, $\rho(y, \gamma, d) = (1/bd)\,v(\gamma)\,\psi(y, d)$, according to Eqns (11) and (12) in the coordinates $\rho/\rho_{\rm m} - y/\Lambda$ as $\gamma \to \infty$ at different grain sizes d, where $\rho_{\rm m} = \beta/bd_{\rm c}k_{\rm a}$, and $d_{\rm c} = 3\beta^3 sl_{\rm b}/16(\beta_{\rm gb} - 1)\,bk_{\rm a}^2$ is the critical size of nanograins above which no microbands are formed [83]. It follows from Eqns (11) and (12) that at $d = d_{\rm c}$, we have $k(d) = 0$ and the dislocation density is distributed in the NC material homogeneously, $\rho(y, d_{\rm c}) = (1/2)\,\rho_{\rm m}$ (Fig. 4a).

At nanograin sizes $d < d_{\rm c}$, the dislocation density is inhomogeneous, forming regions (microbands) with a high dislocation density (Fig. 4b). The smaller the grain size is, the greater the maximum density $\rho_{\rm max} \sim 1/d$ of dislocations in a band. The dislocation density between the bands then remains at the level of $\rho(y, d_{\rm c}) = (1/2)\,\rho_{\rm m}$ (Fig. 4b, dashed line). Figure 4c displays the dependence of the width of shear microbands w on the size of nanograins in NC iron [82]. The curve in Fig. 4c has been plotted in accordance with Eqn (12) at $d_{\rm c} = 350$ nm [83]. The width of the bands becomes infinite at the critical grain size $d = d_{\rm c}$; the dislocation density in the nanograins then remains at the level of $(1/2)\,\rho_{\rm m}$.

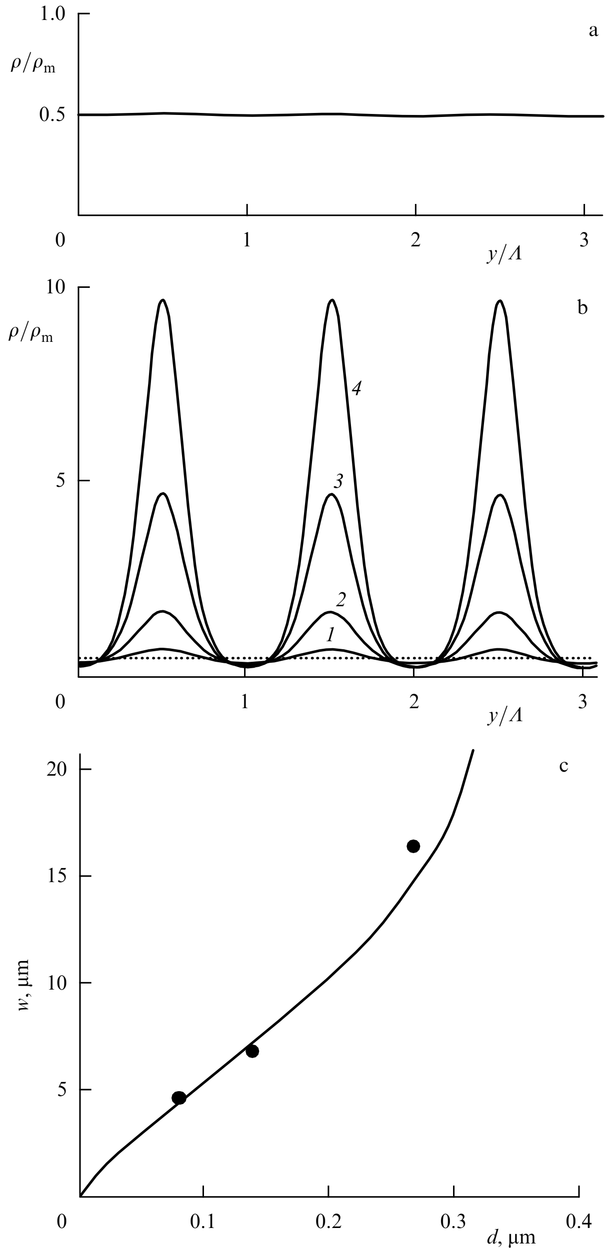

Figure 4. Distribution of the dislocation density ρ in an NC metal in accordance with Eqn (12) at various sizes of nanograins: (a) $d = d_{\rm c}$; (b) $d = 0.9d_{\rm c}$ (*1*), $d = 0.5d_{\rm c}$ (*2*), $d = 0{,}2d_{\rm c}$ (*3*), and $d = 0.1d_{\rm c}$ (*4*); and (c) dependence of the band width w in NC Fe on the size of nanograins [82].

Thus, from the standpoint of dislocation kinetics, the spatial instability of plastic deformation in NC metals in the form of shear microbands arises at a certain quantitative relation between the density of sources of and sinks for dislocations in grain boundaries, and their accumulation and annihilation in the bulk of grains.

We also note, following [64, 80], that a large similarity exists between the shear microbands in NC metals [81, 82] and plastic-flow microbands in amorphous metals (metallic glasses) [110]. In both cases, the bands are oriented in the direction of action of the maximum tangential stresses. This similarity also extends to the type of their stress–strain curves (σ, ε), namely, to the existence of a high initial flow stress and the absence of a subsequent noticeable strain hardening. At the grain size $d = 2-3$ nm, X-ray diffraction reveals continuous diffusion rings in the Ni–W alloy, and only high-resolution electron microscopy allows detecting the existence of clear boundaries of nanograins of such a size [72]. The above circumstances indicate that below the amorphization temperature, the plastic deformation of metallic glasses has a dislocation-like character because of the existence of a short-range order in the amorphous metal and the presence of atomic clusters [111].

2.2 Methods for improving the plastic properties of nanocrystalline metals

The high strength of nanocrystalline and submicrocrystalline (SMC) metals and alloys is accompanied by a strong decrease in the magnitude of the uniform deformation ε_u at which the sample loses plastic stability, and a region of localization of deformation (neck) arises in it, leading to plastic rupture of the sample after a 2–3% tensile deformation. Figure 5 displays the results for NC copper [85] that illustrate this phenomenon. It can be seen that as the yield stress of copper increases (in accordance with the HP relation $\sigma_y \sim d^{-1/2}$), the magnitude of the uniform deformation decreases permanently. The absence of a necessary plasticity resource (quasi-embrittlement) is a significant disadvantage of NC and SMC metals and alloys and prevents their wide practical application under conditions of tensile deformation.

According to the well-known Considére criterion $(\mathrm{d}\sigma/\mathrm{d}\varepsilon \leqslant \sigma)$, the formation of a neck at a progressively lower stage of plastic deformation is favored by an increase in the yield stress, irrespective of the factor responsible for its development, i.e., irrespective of whether this is the alloying [112], a decrease in the grain size (to below 10 μm) [112], the presence of radiation defects [113], or, in the case of bcc metals, an increase in the Peierls stress [114]. One more factor that affects the magnitude of the uniform deformation ε_u is related to the effect of dynamic recovery on the strain-hardening coefficient $\theta = \mathrm{d}\sigma/\mathrm{d}\varepsilon$ at the third stage of stress–strain curves of fcc and bcc metals [112, 114].

The strong sensitivity of nanocrystalline metals to neck formation is related to two circumstances: (1) the above-mentioned significant increase in the yield stress σ_y with grain refinement and (2) a decrease in the strain-hardening coefficient $\mathrm{d}\sigma/\mathrm{d}\varepsilon$ when the grain size becomes less than 1 μm and the mechanism of dislocation multiplication on forest dislocations stops working [40, 87]. Substituting stress (4) at $k_a = 0$ in the Considére condition $\mathrm{d}\sigma/\mathrm{d}\varepsilon \leqslant \sigma$, we find relations for the magnitude of the uniform deformation ε_u and the corresponding flow stress (ultimate tensile stress) σ_u [87]:

$$\varepsilon_u = \frac{1}{m_T k_b}\left[\ln\left(1+\frac{1}{2}\,m_T k_b\right)+\ln\left(1-\frac{\beta_0}{\beta}\,k_b\right)\right], \qquad (13a)$$

$$\sigma_u = \sigma_b\left(\frac{d_b}{d}\right)^{1/2}\left(\frac{m_T/2}{1+(1/2)\,m_T k_b}\right)^{1/2}, \qquad (13b)$$

where $\sigma_b = m_T \alpha \mu (\beta b/d_b)^{1/2}$. According to Eqn (13a), the dependence of the uniform strain ε_u on d is mainly determined by the dependence of the dislocation annihilation coefficient k_b on d, $k_b = (d_b/d)^2$ [see Eqn (1)]. Taking this circumstance into account, the relation $\sigma_y = \sigma(\varepsilon_y) \approx K_y d^{-1/2}$ that follows from Eqn (4) can be written in the parameterized form with respect to the deformation $\varepsilon_u(k_b)$, i.e., $\sigma_y = \sigma_{y0} k_b^{1/4}$, where $\sigma_{y0} = K_y d_b^{-1/2}$. The curve in Fig. 5 has been plotted in accordance with (13a) using the parametric relation between $\varepsilon_u(k_b)$ and $\sigma_y(k_b)$ with the parameter values $\beta_0/\beta = 10^{-2}$, $d_b = 200$ nm, and $\sigma_{y0} = 120$ MPa. This curve demonstrates a quantitative relation between the deformation ε_u and the yield stress of copper. A more detailed analysis of the resistance of metals with micrograined and nanograined structures to neck formation has been performed in [115].

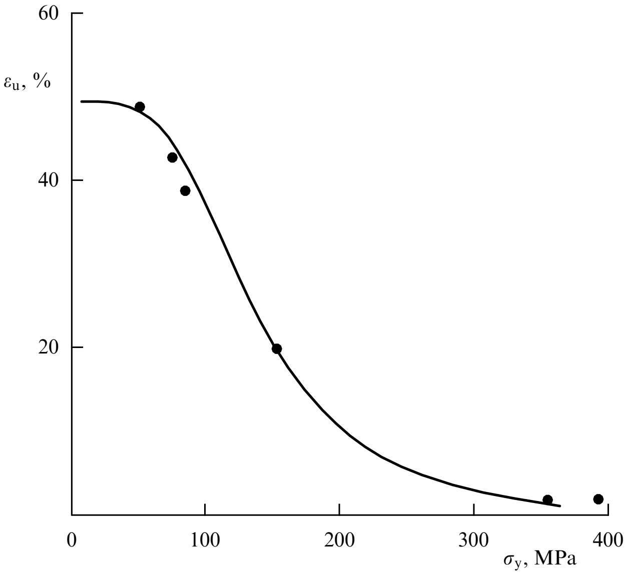

Figure 5. Dependence of the uniform deformation ε_u on the yield stress σ_y during tension of NC Cu [85]. The curve was constructed using Eqn (13a).

2.2.1 Bimodal micro-nano-grained structures.

To improve the plastic properties of nanometals (to increase the uniform strain ε_u), it is necessary to increase their capability of strain hardening. This can be achieved, as was demonstrated in [85–93], by producing mixed (composite) bimodal nano-micro-grained structures that contain a certain fraction of grains of a micron size capable of strain hardening via multiplication of dislocations on forest dislocations and the formation of dislocation cell walls.

In a one-modal micrograined structure of pure metals with grain sizes $d > 1-10$ μm, the evolution of the dislocation density as the degree of deformation increases is determined by the kinetic equation $\mathrm{d}\rho/\mathrm{d}\gamma = k_f \rho^{1/2} - k_a \rho$, where $bk_f \approx 10^{-2}$. As a result, with the initial dislocation density $\rho_0 = \beta_0/bd$, we have the following relation for the flow stress σ [88]:

$$\sigma = m_T \alpha \mu \left[\left(\frac{\beta_0 b}{d}\right)^{1/2} \exp\left(-\frac{1}{2}\,m_T k_a \varepsilon\right) + \frac{bk_f}{k_a}\left(1-\exp\left(-\frac{1}{2}\,m_T k_a \varepsilon\right)\right)\right]. \qquad (14)$$

In a bimodal nano-micro-grained structure, the flow stress, according to the simple rule of mixing, is given by

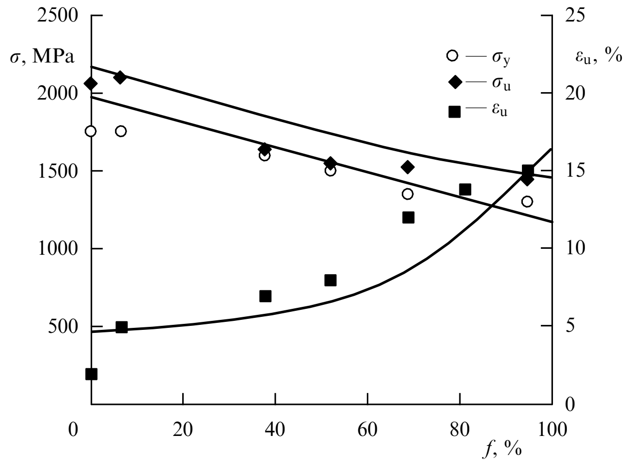

Figure 6. The yield stress σ_y, the ultimate strength σ_u, and the uniform strain ε_u of α-Fe samples with a bimodal micronanograined structure as functions of the volume fraction of micrograins f [91]. The curves were constructed using Eqns (15) with Eqns (4) and (14) taken into account.

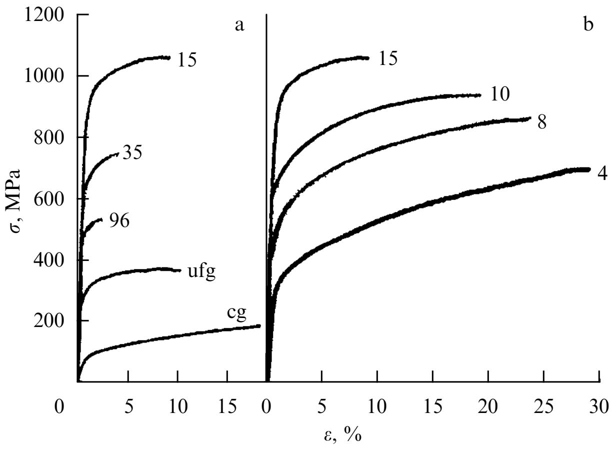

Figure 7. Stress–strain curves of (cg) coarse-grained, (ufg) ultrafine-grained ($d = 450$ nm), and nanotwinned ($\lambda = 4-96$ nm) copper [97]. The figures near the curves show the twin thicknesses λ in nm: (a) $\lambda > 15$ nm; (b) $\lambda < 15$ nm.

$$\sigma(\varepsilon, f) = (1-f)\,\sigma^{(n)}(\varepsilon) + f\sigma^{(m)}(\varepsilon)\,, \tag{15}$$

where f is the volume fraction of micron-size grains and $\sigma^{(n)}$ and $\sigma^{(m)}$ are the flow stresses of single-modal nanograined and micrograined structures according to Eqns (4) and (14).

Figure 6 displays the yield stress, ultimate strength, and uniform strain for a bimodal nano-micro-grained structure in α iron as functions of the volume fraction f of micrograins according to [91]. The curves given in this figure demonstrate the results of numerical calculations of the stresses σ_y and σ_u and of the uniform strain ε_u in α iron according to Eqns (4), (14), and (15) and to the Considére criterion. The calculation was performed for α iron using the parameters $b = 0.25$ nm, $\mu = 83$ GPa, $\beta = 1$, $k_b = 0$, and $bk_f = 2.2 \times 10^{-2}$. The size of the nanograins was 40 nm; the size of the micrograins was 1 μm [91], and the coefficients β_0, α, and k_a were respectively equal to 5.5×10^{-2}, 0.2, 10 and 10^{-2}, 0.4, 3.0 for the single-modal nanograined and micrograined structures. It can be seen from Fig. 6 that at the volume fraction of micrograins $f > 30\%$, the magnitude of uniform strain is 7–8%, which is 3–4 times greater than the strain ε_u in the single-modal NC structure ($\approx 2\%$). Such an increase in the uniform strain is accompanied by a 25% decrease in the yield stress σ_y and ultimate strength σ_u, which is an acceptable result from the practical standpoint. Approximately the same improvement in the plastic properties of nanometals can be achieved in the case of a single-modal nanograined structure by significantly increasing the dispersion of the grain-size distribution [89, 90]. In [87], the question of the improvement of plastic properties of micro-nano-composites was discussed using phenomenological relation for the flow stresses of single-modal components.

2.2.2 Nanotwinned submicrograined structures.

As follows from the results of recent investigations in [94–101, 116–118], efficient means for the enhancement of the plastic and strength properties of NC metals are the strengthening and plastifying effects related to the presence in submicrograined structures of a system of nanotwins with a linear density $1/\lambda$, where $\lambda = 10-100$ nm is the spacing between twin boundaries in submicrograins. In SMC copper, the twin lamellae of the above dimensions are obtained by the method of pulsed electrodeposition of copper from an electrolytic solution of $CuSO_4$ onto a substrate [93, 116]. The formation of nanotwinned (NT) structures is also favored by the plastic deformation of SMC material at low temperatures and by decreasing the energy of stacking faults via the alloying of copper by Al and Zn [98, 117, 118].

Figure 7 displays tensile curves of nanotwinned copper with the grain size $d = 450$ nm, depending on the twin dimension (thickness) λ varying from 4 to 100 nm [97]. It is seen that an optimum combination of strength (1050 MPa) and plasticity (9%) of NC copper is reached at $\lambda = 15$ nm. Figure 8 illustrates the dependence of the yield stress $\sigma_y \equiv \sigma_{0.2}$ of NC copper on the twin thickness λ in the HP coordinates. For comparison, data are also given for NC copper with the grain size varying from 7 to 100 nm. It follows from the comparison of these data that up to the twin thickness 15 nm, the twin boundaries are as efficient a barrier to and source of dislocations as the nanograin boundaries are. This is also

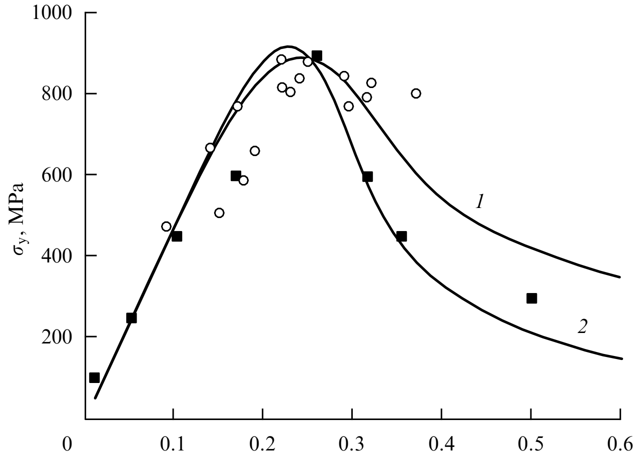

Figure 8. Yield stress σ_y of nanocrystalline [19] and nanotwinned [97] copper as functions of (○) nanograin size d and (■) nanotwin size λ. The meaning of curves *1* and *2* is explained in the main text.

confirmed by the data on the dependence of the SRS coefficient of the flow stress and of the activation volumes of ND copper on the thickness of twin lamellae [98–101]. They are virtually the same as the results for NC copper.

It also follows from the results in Figs 7 and 8 that at the twin thickness less than 15 nm, deviations are observed from the normal HP relation and a significant decrease in the strength of the NT copper occurs, similar to that observed in NC copper and other nanocrystalline metals and alloys with the grain size less than 10–20 nm [39–43]. As was already noted, the mechanism of grain-boundary softening of NC materials remains debatable. Processes such as grain-boundary sliding [5, 47–49], absorption of dislocations by nanograin boundaries (which is accompanied by dislocation annihilation) [4, 40], amorphization of boundaries [80], and saturation of the bulk of nanograins by dislocations emitted from boundaries [39] have been proposed to underlie that mechanism. The breakdown of the HP relation in NT copper adds a new element to this discussion.

According to [97], the observed softening of NT copper at $\lambda < 15$ nm casts doubt on the mechanism of grain-boundary softening of NC copper related to grain-boundary sliding and grain rotation. Naturally, both sliding and rotation occur, but they are a consequence of the absorption of dislocations by grain boundaries, rather than being responsible for these phenomena [4, 40]. We also note that analogous arguments can be applied to the mechanisms of amorphization of boundaries [80] and to the saturation of the bulk of nanograins by dislocations emitted from the boundaries [39]. Based on the data of electron-microscopic investigations, thermoactivation analysis [98–101], and MD simulation of NT copper [120, 121] the authors of [98–101] believe, that the violation of the HP relation at the twin lamellae thickness less than 15 nm is caused by the interaction of lattice dislocations with twin boundaries. This interaction consists of the absorption and emission of dislocations by the boundaries, which leads to the loss of coherency at the twin boundary; as a result, the twin boundaries become similar to conventional grain boundaries.

From the standpoint of dislocation kinetics, the mechanism of grain-boundary softening of NC metals due to the absorption of dislocations by nanograin boundaries and dislocation annihilation in the boundaries has been considered in [4, 40] and is discussed in this review (see Section 2.1). In Figure 8, curve *1* demonstrates the dependence of the yield stress of NC copper given by Eqn (4) at $\varepsilon_y = 0.2\,\%$, $k_b = (d_b/d)^2$, $d_b = 180$ nm, $b = 0.26$ nm, $\beta_0 = 10^{-2}$, $\alpha = 0.5$, and $\mu = 48$ GPa. The $k_b \sim d^{-2}$ dependence means that the absorption of dislocations by grain boundaries is accompanied by the annihilation of dislocations of opposite signs in the boundary via the mechanism of their diffusional climb [40]. Upon diffusional dissolution of single dislocations in the boundary, the dependence of the annihilation coefficient on the grain size has the form $k_b' = (d_b'/d)^3$ [40]. Curve *2* in Fig. 8 shows the $\sigma_y(d)$ dependence $k_b' \sim d^{-3}$ at $d_b' = 80$ nm, with the other parameters being the same as for curve *1*. It can be seen that this dependence is close to the experimental dependence of the yield stress of NT copper $\sigma_y(\lambda)$ at the twin lamellae sizes $\lambda < 15$ nm. This circumstance can serve as an argument in favor of the mechanism of softening of NT grain structures via the diffusional absorption (dissolution) of lattice dislocations by (in) twin boundaries. It has been established in [122] that the diffusion along incoherent twin boundaries in copper does not differ significantly from the diffusion along conventional grain boundaries.

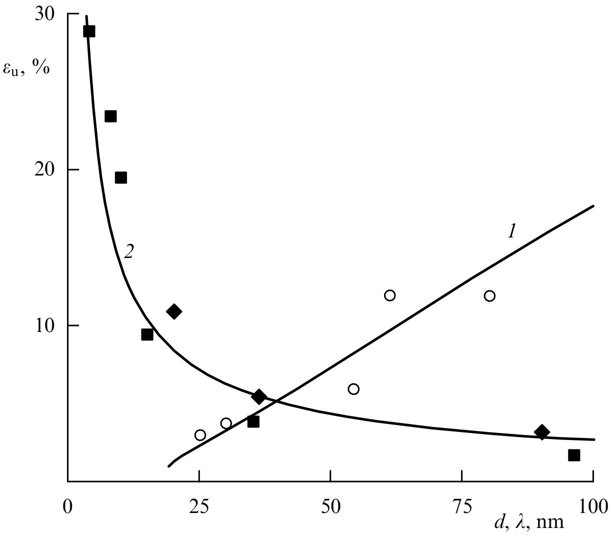

Figure 9. Variations of the uniform strain ε_u before neck formation in nanocrystalline [98] and nanotwinned [96, 97] copper, depending on (○) the nanograin size d and (■, ◆) the nanotwin thickness λ.

One specific feature of NT copper compared to the NC copper is the enhanced resistance to neck formation (see Fig. 7). Figure 9 displays data on the dependence of the deformation ε_u corresponding to the start of neck formation on the nanograin size d and nanotwin thickness λ in NC [98] and NT [96, 97] copper. It can be seen that these dependences have opposite characters. Curve *1* in Fig. 9 demonstrates the result of calculations of the uniform strain ε_u in NC copper via Eqn (13a). Good agreement between the theory and experiment is observed. An analysis shows that based on the Considére criterion alone, it is impossible to substantiate the enhanced stability of ND SMC structures to neck formation in terms of the dislocation-kinetics theory or to establish a quantitative connection between the size of twins λ and the uniform strain ε_u (see Fig. 9).

Finding this connection, as is noted in [101], requires that not only the coefficient of the strain sensitivity of the flow stress $n = \mathrm{d} \ln \sigma / \mathrm{d} \ln \varepsilon$ but also the SRS coefficient of the flow stress $m = \mathrm{d} \ln \sigma / \mathrm{d} \ln \dot{\varepsilon}$ be taken into account in the modified Hart relation [123]

$$\varepsilon_u = \frac{\exp(n)}{\left[1 - (1 - \Delta_0)^{1/m}\right]^m} - 1\,, \tag{16}$$

where Δ_0 is the magnitude of the initial geometric reduction of the cross section of the tensile specimen. It follows from Eqn (16) that the increase in the SRS coefficient imparts additional stability to the process of tensile deformation of the sample, leading to an increase in the uniform strain ε_u in excess of the value specified by the Considére criterion. Indeed, substituting the SRS coefficient for the yield stress (6c) in the form of its dependence on the twin thickness $m = m_d\left(1 + (\lambda_y/\lambda)^{1/2}\right)$, we obtain, at $n = 0$, $\Delta_0 = 0.01$, $m_d = 5 \times 10^{-3}$, and $\lambda_y = 1.5$ µm, a result that agrees with the experiment (see Fig. 9, curve *2*).

Summarizing the performed dislocation-kinetics analysis of the strength and plastic properties of NC metals, we can conclude that dislocations play the decisive role in the explanation of all features of the mechanical behavior of these materials.

3. Size effects under deformation of micro- and nanocrystals

The first results of investigations of the effect of the size factor on the strength of crystals were obtained more than five decades ago [13, 14, 124]. It was established in tensile tests of thin single crystals of copper that the yield stress of samples with a cross section of 120 μm is significantly greater than that of single crystals with $D > 500$ μm [124]. The experiments with the deformation of dislocation-free microcrystals (metallic whiskers) of Cu, α-Fe, and Ag, 5 to 20 μm in diameter, showed that their strength (yield stress) approaches the theoretical shear strength equal to $\mu/10-\mu/20$ [13–15].

In the 1960s, a number of other effects related to the influence of the size factor on the strength and deformation behavior of metallic crystals were revealed. In tensile tests of copper microcrystals (whiskers) with a diameter $D < 20$ μm [125] it was established that at the second (linear) stage of their stress–strain curves, the strain hardening (SH) coefficient $\theta_2 = \mathrm{d}\tau/\mathrm{d}\gamma$ decreases strongly and approaches the SH coefficient θ_1 of the first stage (stage of easy slip) at $D = 5-10$ μm. Thus, it has been demonstrated that a thinning of a crystal favors the disappearance of the second stage of SH and leads to the appearance of the first stage with a lower SH coefficient, similar to what occurs in bulk copper crystals in passing from the tensile axis [100] and [111] to [110].

The appearance and disappearance of the first stage of SH in thin crystals is also affected by the surface of the crystal. The presence of a strong oxide film on the surface [128], a special coating [129], or a subsurface layer strengthened in one way or another [130, 131] favors the accumulation of dislocations in the crystal, an increase in the SH coefficient, and the disappearance of the first stage. By contrast, a treatment of the crystal surface that facilitates the escape of dislocations from the crystal, e.g., by using electrolytic or chemical etching of the surface in the process of deformation, leads to a decrease in the deforming stress and the appearance of a stage with a low SH coefficient [132, 133].

In terms of the dislocation-kinetics approach, the above-noted size effects in crystals with cross sections $D > 100$ μm have been quantitatively analyzed in [127, 134] (see also review [56]). In Section 3, in terms of an analogous approach, we analyze the size effect in crystals with transverse dimensions 0.1–10 μm in the absence (Section 3.1) and in the presence (Section 3.2) of a nominal gradient of plastic deformation.

3.1 Strength and plasticity of micro- and nanocrystals

3.1.1 Tensile and compressive curves of macro-, micro-, and nanocrystals. Figure 10 illustrates, in the shear stress–shear strain (τ–γ) coordinates, the tensile curves for copper single crystals of thickness $D = 0.1-2$ mm with a tensile axis [100] [124]. Figure 11 shows tensile stress–strain curves of copper whiskers with cross sections $D = 5-20$ μm [125]. Along with the well-known data of Brenner [13, 14], these curves demonstrate the first results of the investigations of the effect of size factors on the shape and parameters of the curves of strain hardening of crystals with transverse dimensions $D > 1$ μm. It follows from the data in Fig. 10 that the length of the first (easy-slip) stage in the tensile curve increases with a thinning of the crystal, and the SH coefficient θ_2 at the second stage decreases for crystals with $D = 0.12$ and 0.2 mm.

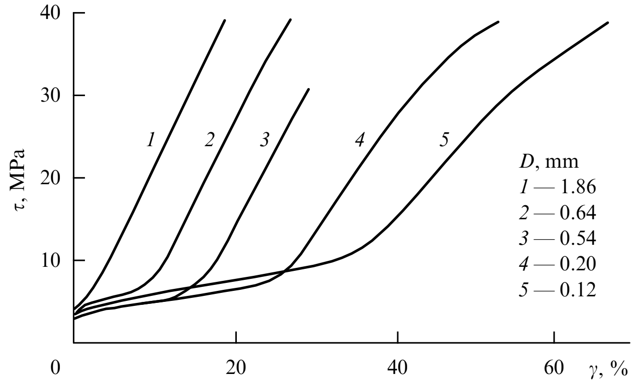

Figure 10. Tensile stress–strain curves of copper single crystals with different cross sections D upon loading along the [001] direction [124].

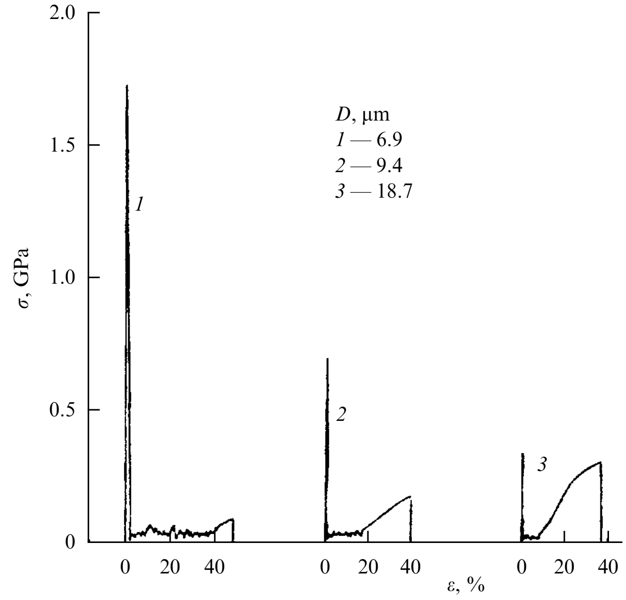

Figure 11. Tensile stress–strain curves of copper microcrystals (whiskers) with different cross sections D. Loading along the [111] direction.

This decrease is especially noticeable in the tensile curves of microcrystalline copper (see Fig. 11). Each of the $\sigma-\varepsilon$ curves shown in this figure consists of three characteristic segments: a yield peak ('tooth') related to the small initial density of dislocation sources in the crystal, a yield plateau, and the region of the second stage of SH. It is seen that the SH coefficient at the second stage of SH ($\Theta_2 = \mathrm{d}\sigma/\mathrm{d}\varepsilon = \theta_2/m_{\mathrm{Sm}}^2$) decreases upon thinning the crystal (m_{Sm} is the Schmid factor). Figure 12 illustrates this observation with the experimental dependences of the coefficients θ_1 and θ_2 on the transverse dimensions of Cu crystals in the ($\theta/\theta_{\mathrm{II}}$, D) coordinates. Here, $\theta_{\mathrm{II}} \approx (2-2.5) \times 10^{-3}\mu$ is the SH coefficient at the second stage of the tensile curves of bulk fcc crystals [135]. According to [124], $\theta_{\mathrm{II}} = 200$ MPa in copper. Black dots in the figure denote the relative values of the coefficient $\theta_2/\theta_{\mathrm{II}}$ in copper microcrystals (whiskers) [125]; white squares and white circles are the values of the coefficients θ_2 and θ_1 in relatively thin ($D = 0.1-1$ mm) copper single crystals [124].

It follows from the results in Fig. 12 that the SH coefficient at the easy-slip stage is an order of magnitude smaller than the coefficient θ_2. Another conclusion that can be made from these data is that $\theta_2 \approx \theta_1$ for crystals with $D = 5-10$ μm. This means that the second stage of strain hardening, which is related to the multiplication of moving dislocations on forest

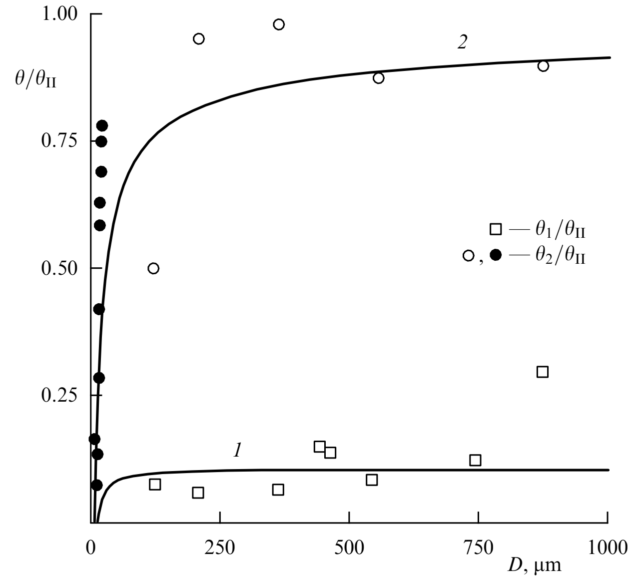

Figure 12. The coefficients θ_1 anf θ_2 of strain hardening at the first [124] and second [124, 125] stages of the tensile curve of micro- and macrocrystals of copper as functions of their cross sections D in the $(\theta/\theta_{\rm II}, D)$ coordinates.

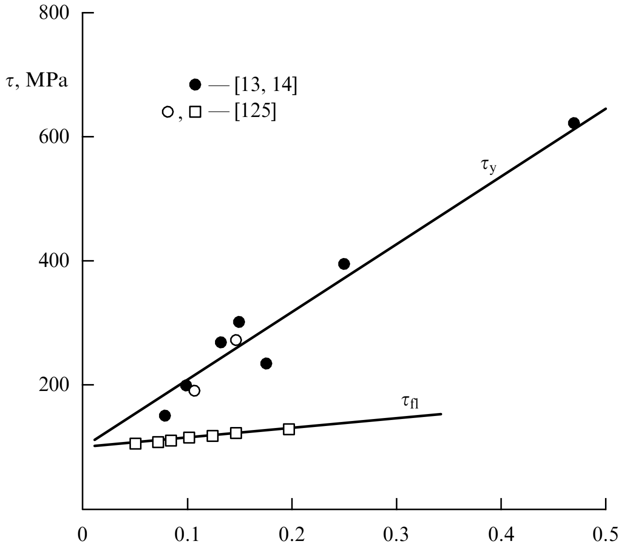

Figure 13. The yield stress $\tau_{\rm y}$ and flow stress $\tau_{\rm fl}$ of copper single crystals [13, 14, 125] as functions of their cross section D in (τ, D^{-1}) coordinates.

dislocations in noncoplanar slip planes, is virtually absent in such microcrystals.

It also follows from Fig. 11 that the magnitude of the yield point $\tau_{\rm y}$, the flow stress $\tau_{\rm fl}$, and the shear $\gamma_{\rm L} = \varepsilon_{\rm L}/m_{\rm Sm}$ at the yield plateau increase as the transverse dimension of a microcrystal decreases. Figure 13 demonstrates the dependences of these stresses on the transverse dimension in (τ, D^{-1}) coordinates. Along with the data in [125], the figure also shows Brenner's results [13, 14] for the stress $\tau_{\rm y}$ in copper microcrystals. The straight lines in Fig. 13 correspond to empirical relations like

$$\tau_{\rm y} = \tau_0 + k_{\rm y}\,\frac{\mu b}{D}\,, \quad \tau_{\rm fl} = \tau_0 + k_{\rm fl}\,\frac{\mu b}{D}\,, \tag{17}$$

where the coefficients $k_{\rm y}$ and $k_{\rm fl}$ are respectively equal to 93 and 13, and $\tau_0 = 100$ MPa. An analogous relation, $\tau_{\rm y} = \tau_0 + k_{\rm y}(\mu b/D)$, where $k_{\rm y} = 280$ and $\tau_0 = -0.4$ GPa, holds in microcrystals of α-Fe for the stress at the upper yield point $\tau_{\rm y}$ [13, 14].

It was also found in [125] that in copper whiskers, the dependence of the deformation at the yield plateau on the microcrystal dimension obeys the equation $\varepsilon_{\rm L} = 1.67/D$, where D is measured in microns. The shear deformation at the yield plateau $\gamma_{\rm L} = \varepsilon_{\rm L}/m_{\rm Sm}$ can be written in the compact form $\gamma_{\rm L} = D_{\rm L}/D$, where $D_{\rm L} = 1.67/m_{\rm Sm} \approx 3.3$ μm at $m_{\rm Sm} = 0.5$. Assuming further that the stress $\tau_{\rm fl}$ and the shear deformation $\gamma_{\rm L}$ at the yield plateau are related as $\tau_{\rm fl} - \tau_0 = \theta_2\gamma_{\rm L}$, we theoretically estimate the characteristic dimension of the microcrystal section $D_{\rm L}$ as $D_{\rm L} = k_{\rm fl}(\mu/\theta_2)\,b$. As can be seen from Fig. 12 (solid circles), at $D \approx 20$ μm, the coefficient $\theta_2 \approx 0.75\,\theta_{\rm II}$, and its magnitude decreases with decreasing the crystal cross section. Assuming that $\theta_2 \approx 0.5\,\theta_{\rm II}$ on average and taking $\theta_{\rm II}/\mu = 2.5 \times 10^{-3}$ [135], $k_{\rm fl} = 13$, and $b = 0.256$ nm, we estimate the characteristics dimension as $D_{\rm L} \approx 2.7$ μm, which is close to the experimental value.

Thus, the analysis of the results of the first stage of the investigation of the effect of size factors on the strength and deformation behavior of crystals with transverse dimensions D in the range 5–100 μm shows that this influence is significant and affects the shape of the strain-hardening curves of crystals and their parameters, and leads to an enhanced sensitivity of small-size crystals to the state of their surface.

A new period in the investigation of the effect of transverse dimensions of crystals on their strength and deformation (plastic) properties, as was already noted in the Introduction, began several years ago with the development of an efficient method of fabrication of crystals with transverse dimensions $D < 1$ μm in the form of micropillars by etching the surface of a macrocrystal by a focused ion beam [16–18, 136] or by lithographic etching of thin metallic films deposited on a substrate [19, 137].

The first experiments on the compression of micropillars using nanoindenters with a flat punch were performed on microcrystals of nickel [16] and gold [17]. To date, a large group of metals has been studied in various detail, in particular, fcc metals such as Ni [16, 136, 138–141], Au [17, 18, 142–148], Cu [149–153], Al [137, 154–156], Ag [157, 158], bcc metals Mo [148, 159–167], Nb [164, 165, 167], W [164, 167] Ta [164, 167], V [168], and microcrystals of the $\rm Ni_3Al$ alloy and alkali-halide LiF [169, 170]. The most thoroughly studied at present are microcrystals and nanocrystals of nickel, gold, and molybdenum. Figure 14 depicts samples of micropillars of gold 660 nm in diameter and 2.14 μm in height in the initial state and after deformation to 10 and 20% [17, 18]. We note that just as in crystals with $D > 1$ μm, slip lines are observed on the surface of deformed crystal with $D < 1$ μm, especially well visible after significant plastic deformation (Fig. 14c).

Figure 15 demonstrates compressive stress–strain curves of Ni micropillars with the orientation of the compressive axis [111] and with the micropillar diameter varying in a wide range (from 165 to 1970 nm) [139]. It can be seen that as the crystals are thinned, their flow stresses increase strongly; the discreteness of slip also increases, which follows from the presence of deformation jumps in the curves. The steplike (serrated) character of the curves is related to the fact that the

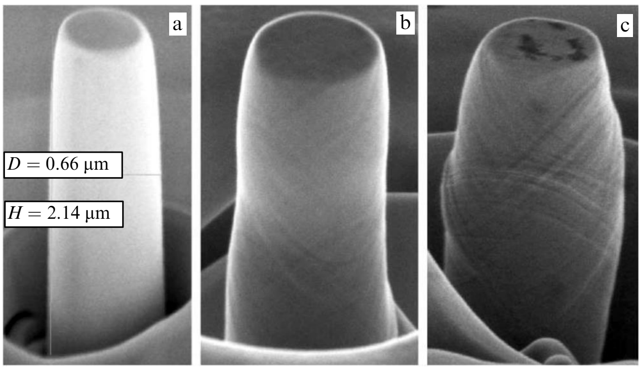

Figure 14. Gold microcrystals 660 nm in diameter and 2.14 μm in height: (a) in the initial state and after compressive deformation to (b) 10 and (c) 20% [17, 18].

deformation of the crystal in the nanoindenter is performed at constant velocity of the applied load (soft regime of loading). Under conditions of a constant rate of deformation (rigid mode of loading), the compressive curves acquire a saw-like shape [18, 141, 157].

Figure 15b displays the results of the processing of the compressive curves of Ni crystals shown in Fig. 15a. Curves *1* and *2* demonstrate the dependences of the shear flow stress $\tau = m_{\mathrm{Sm}}\sigma$ on the diameter D of micropillars at two degrees of deformation, 0.2 and 15%. The first stress can be regarded as the stress τ_{y} corresponding to the beginning of plastic deformation of the nanocrystal; the second stress corresponds to the state of developed plastic flow. Within the spread of experimental data, the dependences under consideration can be approximated by a relation of the type

$$\tau_{\mathrm{y}} = k_{\mathrm{y}}\left(\frac{b}{D}\right)^{n}\mu\,, \quad \tau_{\mathrm{fl}} = k_{\mathrm{fl}}\left(\frac{b}{D}\right)\mu\,, \tag{18}$$

where $n = 0.9$, $k_{\mathrm{y}} = 2.3$, and $k_{\mathrm{fl}} = 13.3$. We note that the second relation in (18) is analogous to the second relation in (17) for the flow stress τ_{fl} of Cu microcrystals (whiskers) upon deformation at the yield plateau to about 10–40% (see Fig. 11).

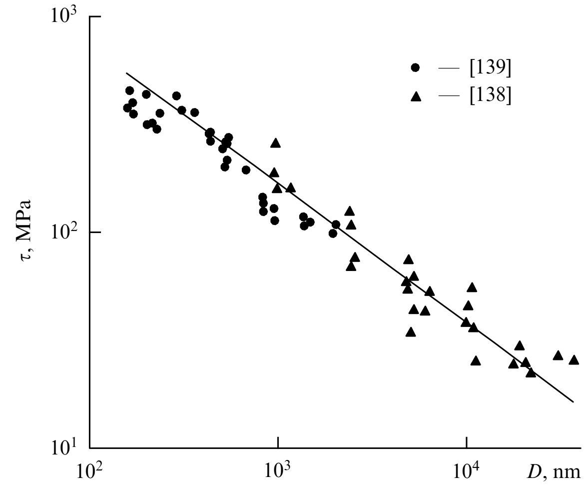

Figure 16. Dependence of the flow stresses of nickel nano- and microcrystals as functions of the cross section D at $\varepsilon = 3\%$ [138, 139].

At deformations $\varepsilon > 10\%$, dependences analogous to the second relation in (18) are also observed in microcrystals and nanocrystals of Au [148] and Ag [157] with the coefficient k_{fl} varying in narrow limits (11–13). As regards the stresses at deformations $\varepsilon \leqslant 3\%$, it can be noted that according to [138, 139, 144, 147], the average values for fcc metals are $n \approx 0.67$ and $k_{\mathrm{y}} \approx 0.6-0.7$ (Fig. 16). For bcc nanocrystals of Mo [148], Nb [164], and V [168] at $D = 100$–1000 nm and deformations $\varepsilon \leqslant 3\%$, these parameters are $n = 0.8-1.0$ and $k_{\mathrm{y}} = 3-6$; there are also separate results for micropillars of W, Ta, and Nb with $n = 0.4-0.5$ [164, 167]. In LiF microcrystals [169], $n = 0.74$, $k_{\mathrm{y}} = 4$ [58].

A special case is presented by dislocation-free microcrystals (whiskers). According to the data in Fig. 13, the exponent n in relation (17) for the yield stress of dislocation-free copper and iron whiskers is equal to unity. The coefficients $k_{\mathrm{y}} = 93$ (Cu) and 280 (Fe) in dislocation-free crystals are substantially greater than the coefficients $k_{\mathrm{y}} \approx 1$ for crystals containing an initial density of defects, such as dislocations or ledges on the crystal surface [see (18)]. In specially prepared dislocation-free and defect-free Mo micropillars [159, 160, 163], the deformation diagrams have a catastrophic character, just as in the case of copper microcrystals (whiskers) (see Fig. 11). The stress for the beginning of plastic deformation (the upper yield stress) in them reaches the theoretical shear strength

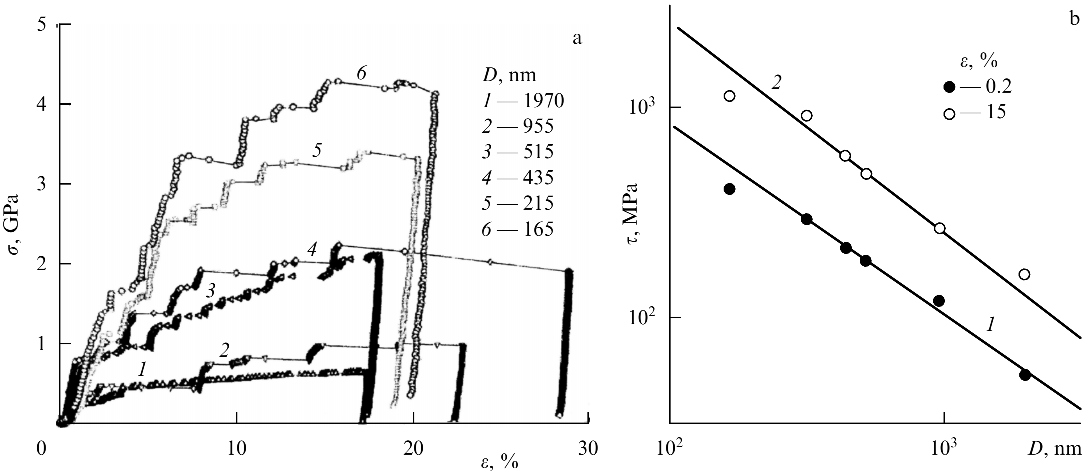

Figure 15. (a) Stress–strain curves of Ni micropillars of various diameter compressed in the [111] direction [139] and (b) dependences of the yield stress $\tau_{0.2}$ and the flow stress τ_{fl} of micropillars at $\varepsilon = 15\%$ on the micropillar diameter $D\varepsilon = 15$.

equal to $\mu/20$ and stops depending on the transverse dimensions of the crystal [159, 160].

Thus, the investigations of crystals with the transverse dimensions 100–1000 nm shows that the previously revealed features of deformation of crystals with cross sections $D = 1-20$ μm are even enhanced in the nanorange. The strength of crystals continues growing with decreasing D, both in the first stage of deformation (see Fig. 16) and in the stage of developed plastic flow (Fig. 15b); after initial strong growth of the flow stress, the stress–strain curves exhibit a tendency to saturation in the absence of the second stage of strain hardening (Fig. 15a); the discrete character of slip and the sensitivity of crystals to surface defects also increase.

3.1.2 Mechanism of the influence of the size factor. The above results have been the subject of experimental investigations (transmission electron microscopy [139, 141, 155, 163, 171, 172], computer 3D-DDD (3D discrete dislocation dynamics) [51–55, 173–175], and MD [176–178] simulations, and have also been analyzed in terms of dislocation-kinetics [58, 136] and statistic [179, 180] approaches aimed at the establishment of the mechanism(s) of the influence of crystal size on its strength and deformation behavior.

The discussion of the first results [17, 18, 142] of the plastic deformation of micropillars led the authors to the conclusion that the high strength of micropillars is related to the necessity of activating Frank–Read (FR) dislocation sources with shorter and shorter critical lengths in the process of deformation of nanocrystals and microcrystals. The dislocations generated by the sources escape from a thin crystal through its surface without multiplication and interaction with one another, such that the crystal subjected to deformation suffers ''dislocation starvation.''

The authors of [16, 138] also noted that in the compression stress–strain diagrams of micropillars, the initial stage of strong strain hardening is replaced by a stage with a very low strain-hardening coefficient. The strain-hardening exhaustion is related in [16, 138] to the exhaustion of the capability of dislocation sources to emit dislocations. The mechanisms of dislocation starvation [142] and dislocation-source exhaustion [138] as the factors responsible for the high strength of nanosized crystals were later widely discussed, checked, and refined using electron-microscopic data and results of 3D-DDD simulation.

Two important questions arise in discussing stress–strain diagrams of micro- and nanocrystals (Fig. 15a) and results of electron-microscopic observations and of 3D-DDD simulation: (1) how does the dislocation density ρ change in micro- and nanocrystals when their cross section decreases; and (2) whether the flow stress of the crystal obeys the Taylor relation $\tau = \alpha\mu b\rho^{1/2}$.

The TEM investigation of the defect structure of micro- and submicrocrystals prepared by etching the surface of the parent crystal using a focused ion beam showed that the subsurface layer of micropillars with a thickness of several dozen nanometers contains intrinsic dislocation loops formed upon the penetration of Ga^+ ions into the bulk of the crystal [139, 141, 163]. After a moderate plastic deformation, these loops disappear, being swept by moving dislocations, and escape from the crystal, exerting no significant effect on its strength. A 3D simulation of this process [173] confirmed the insignificant role of these loops in the mechanism underlying the effect of the size factor on the strength of nanosized crystals with $D > 100$ nm. But it seems to be premature to completely exclude these loops as potential FR sources [139]. For example, upon compression of Mo nanocrystals with a diameter of 91 nm in situ, in the column of an electron microscope, it has been demonstrated [163] that after the preliminary removal of these defects by annealing, the strength of the crystals increases sharply and reaches the theoretical shear strength equal to $\mu/10$ [181]. Another consequence of high annealing is the diffusional elimination of irregularities on the crystal surface and smoothing of angles on its loaded end, which can serve as stress concentrators and dislocation sources.

With 3D-DDD simulations of the process of plastic deformation of nanosized crystals [53, 55, 174, 175, 182], it has been revealed that the FR dislocation sources in them are predominantly single-pole, having one point of pinning located inside the crystal and a free end at its surface. Their appearance is related to the fact that the crystal surface truncates [53] part of the dislocation loop generated by a two-pole dislocation source (having two pinning points). It is obvious that the least strong and most efficient (from the standpoint of the emission of dislocations) source is the one with an end pinned near the center of the crystal. But because sources with even shorter critical lengths can also exist near the crystal surface, the stress that is required for the activation of single-pole sources is in the general case given by

$$\tau_{\mathrm{FR}} = \frac{\mu b}{\delta_{\mathrm{S}} D}\,, \tag{19}$$

where $\delta_{\mathrm{S}} < 1$ is a coefficient that takes the distance from the pinning point to the crystal surface into account.

In investigating the dislocation structure in Ni crystals [140], it was revealed that as the cross section of a crystal decreases from 10 μm to 1 μm, the dislocation density increases by an order of magnitude, from 10^{13} m^{-2} to 10^{14} m^{-2}. This increase occurs at the initial stage of deformation, within 3–10%; under further deformation, up to the degree of deformation equal to 50%, the dislocation density remains constant, just as the flow stress does. An estimation shows that at $\rho = 10^{14}$ m^{-2}, $b = 0.25$ nm, $\mu = 75$ GPa, and $\alpha = 0.5$, the flow stress is equal to 94 MPa according to the Taylor relation and only moderately differs from the experimental value $\tau \approx 100$ MPa for a crystal with $D = 1$ μm [140] (see Figures 15b and 16). According to (19), the stress required for the start of a single-pole FR source in such a crystal, τ_{FR}, is equal, at the coefficient $\delta_{\mathrm{S}} = 0.2$, to the same value as the stress τ defined by the Taylor relation.

At crystal cross sections less than 1 μm, the situation is by no means unambiguous. The flow stresses reached in such crystals are 1–2 GPa at $D \approx 100$ nm (see Figs 15 and 16). The electron-microscopic data [139, 171] and the results of a 3D simulation [53] show that the dislocation density in a deformed crystal with $D < 1$ μm after unloading is insufficient to explain the observed level of flow stresses according to the Taylor formula. According to that formula, at the thickness of an Ni crystal given by 165 nm (Fig. 15b), the flow stress $\tau \approx 1000$ MPa should correspond to the dislocation density $\rho \approx 10^{16}$ m^{-2}. This is substantially greater than the dislocation density experimentally observed in the crystal after unloading [139].

The 3D simulation in [53] of the deformation of Ni crystals 1 μm thick revealed that the process of plastic deformation in a thin crystal consists of a periodic emission of groups of dislocations from dislocation sources and the subsequent escape of part of the dislocations from the crystal through its surface. As a result of the cyclic, dynamic character of this process, two different densities of dislocations arise in the crystal: in the process of generation of dislocations from the source and after their complete or partial relaxation (escape from the crystal). It is obvious that the magnitude of the flow stress is determined by the higher dislocation density related to their generation from the sources.

The dynamic character of the evolution of the dislocation density was confirmed by in situ experiments, with the observation of the process of deformation of Ni nanocrystals 290 nm thick [141] and Al crystals of submicron sizes [171] in a transmission electron microscope. The dislocations generated by the sources almost completely escaped from the crystal, but the dynamic process of their generation from the sources led to their cyclic appearance in the course of continuing loading, thus determining the high level of stresses at the stage of dislocation generation from the sources and upon their motion to the crystal surface.

The stress for the start of dislocation generation from the FR sources in an Ni crystal at $D = 100$ nm in accordance with Eqn (19) is 940 MPa (at $\delta_S = 0.5$), which is close to the flow stresses shown in Fig. 15b at deformations corresponding to the start of plastic deformation ($\varepsilon = 0.2\%$). On the other hand, it is also seen from Fig. 15 that at the deformation magnitude equal to 15%, the flow stress is twice as large as at $\varepsilon = 0.2\%$. The question is: what determines the magnitude of this stress and, on the whole, the process of strain hardening before the stress reaches a constant level as a result of a balance established between the rate of generation of dislocations from the sources and their escape from the crystal through its surface?

According to the mechanisms of dislocation starvation and source exhaustion, this should be related to the activation of sources with progressively shorter critical lengths. But then the following question arises: did these sources exist in the initial crystal or do they appear in the process of its deformation as a result of the formation, for example, of ledges on its surface due to the emergence of screw components of dislocation loops onto this surface [183]? Observations of the deformation of Al crystals of submicron sizes in an electron microscope show [171] that new single-pole sources with shorter activation lengths form in the process of deformation as a result of cross slip of screw segments of dislocation loops and the formation of points of pinning of dislocations upon the interaction of dislocations belonging to different slip systems. Multiple slip is a characteristic feature of the deformation of thin crystals because of the breakdown of the Schmid law in them [127, 154]. As a result of these processes, the flow stress of the crystal increases.

If the dislocation sources arise in the process of deformation, then the Taylor relation can be written as $\tau = \alpha\mu b/l$, where $l = \rho^{-1/2}$ and ρ is the density of sources. In this form, the stress τ can be considered the stress for the start of single-pole sources τ_{FR} in Eqn (19). Equating τ to this tress, we obtain a relation for the effective length $l = \alpha\delta_S D$ and the density of sources $\rho = l^{-2} \sim D^{-2}$.

Therefore, stresses (17) and (18) depend not only on the critical size of dislocation sources but also on their number (density) in the crystal. In the absence of dislocation sources, the shear strength of a crystal is determined by the shear stability of the lattice [181] and is independent of the crystal size [159, 160]. But in the presence of defects, e.g., ledges on the crystal surface [174] or dislocation sources existing in the initial state of the crystal [163] or created by its preliminary deformation [160, 163, 184], the shear strength of the crystal decreases and becomes dependent on its size, and the dependence is the stronger, the thinner the crystal and the smaller the density of dislocation sources in it.

In the quantitative relation, the results of 3D-DDD simulation are in agreement with the experiment and exhibit fine details, such as the above-noted formation of single-pole dislocation sources, the effect of cross slip of dislocations [182, 185, 186], and the effect of surface coating [175] on the dislocation density in a microcrystal. At the same time, being a virtual analog of dislocation-kinetic processes that develop in real microcrystals, the 3D simulation, without using theoretical models, is incapable of explaining the experimentally observed dependences of the strength of micro- and nanocrystals on their transverse dimensions in form (18) or of estimating the values of the exponents $n = 0.6-1.0$ and the coefficients k_y and k_{fl} in these relation. For this, a more consistent and systematic approach to the analysis of the experimental data given in Sections 3.1.1 and 3.1.2 is required.

3.1.3 Dislocation-kinetics analysis of the size factor. In our opinion, such an approach can be provided by analyzing the mechanism of the influence of the size factor from the standpoint of dislocation kinetics. This approach has already been used in Section 2 for the analysis of the effect of grain size on the strength and plastic properties of micro- and nanocrystalline materials. Previously, this approach was also successfully used in [56, 134] for the analysis of the effect of various structural factors, including the size factor [127], on the multistage character and the parameters of curves of strain hardening of macrocrystalline samples of fcc metals. In [127], the analysis of the size factor in copper single crystals [124] was restricted to their transverse dimensions in the range 0.1–1.0 mm. In this section, this approach is extended to the range 0.1–100 μm.

The dislocation-kinetics approach is based on the kinetic equation that describes the rate of change in the dislocation density $\mathrm{d}\rho/\mathrm{d}\gamma$ as the shear deformation γ increases, with the structural features of a crystal and the kinetic processes characteristic of an ensemble of dislocations in it, such as generation of dislocations from sources, multiplication, annihilation, and immobilization of dislocations, taken into account. Applied to the problem considered in this section, this equation is written as [58]

$$\rho\,\frac{\mathrm{d}\rho}{\mathrm{d}\gamma} = \left(\frac{n_V}{b} + \frac{n_S}{bL_{FR}}\right) + \left(k_m - k_{im} + k_f\,\rho^{1/2}\right)\rho - k_a\rho^2\,. \tag{20}$$

The right-hand side contains terms that are responsible for the processes of generation, multiplication, immobilization, and annihilation of dislocations, whose rate, as was already said above, is sensitive to structural and size factors. The terms in the first parentheses in Eqn (20) describe the generation of dislocations from the dislocation sources in the bulk of the crystal (with a density n_V that is independent of the crystal size) and from the surface sources (with critical lengths $L_{FR} = \delta_S D$ and a density n_S that depends on the transverse dimensions). The density of surface and subsurface dislocation sources depends on the technology of the production of crystals of various transverse dimensions. It specifies the quality of the surface, i.e., the number and magnitude of ledges on the surface, which serve as stress concentrators and sources of dislocations. The number N_S of subsurface single-pole FR dislocation sources on the perimeter of a slip plane is $\pi D/m_e L_{FR}$, where $m_e = \sin\varphi$ and φ is the angle between the slip plane and the loading axis. The sources are distributed in a subsurface layer of the area

$$S = \frac{\pi}{4m_e^2}\left[D^2 - (D - m_e L_{FR})^2\right] \approx \frac{\pi}{2m_e} D L_{FR}\,.$$

As a result, we can express the density of subsurface sources as

$$n_S = \frac{N_S}{S} = \frac{2}{L_{FR}^2}\,.$$

The terms in the second parentheses in Eqn (20) describe the processes of dislocation multiplication (due to double cross slip) on obstacles of a nondeformation origin (such as precipitates or clusters of impurity atoms, where $k_m = 1/b\lambda_m$ and λ_m is the dislocation free path between these obstacles) and a deformation origin (e.g., forest dislocations, $k_f = \delta_f/b$, $\delta_f \approx 10^{-2}$), as well as the immobilization of dislocations on obstacles of various types ($k_{im} = 1/b\lambda_{im}$, where λ_{im} is the spacing between such obstacles). It is obvious that the generation of dislocations from sources and their multiplication on various obstacles increase the dislocation density in the crystal, whereas the immobilization of dislocations and the annihilation of screw segments of dislocation loops via cross slip (the last term in the right-hand side of Eqn (20), $k_a = h_a/b$, where h_a is the effective length for the annihilation of screw dislocations [186]) decrease the rate of multiplication and therefore reduce the dislocation density.

In the right-hand side of Eqn (20), the transverse dimensions of the crystal D can affect not only the density of subsurface dislocation sources n_S but also the coefficient of the immobilization of dislocations k_{im}, because the escape of dislocations from a thin crystal through its surface leads to the withdrawal of dislocations from the process of their multiplication. The dislocation path through the crystal with the orientation of the slip plane taken into account is determined by the expression $L_e = D/m_e$. As a result, we can express the coefficient k_{im} as $k_{im} = m_e/bD$. Substituting the above dependences of n_S and k_{im} on D in Eqn (20), we obtain

$$\rho\frac{d\rho}{d\gamma} = \frac{\eta_S}{bD^3} - \frac{m_e}{bD}\,\rho + k_f\rho^{3/2} - k_a\rho^2\,, \tag{21}$$

where $\eta_S = 2/\delta_S^3$. In the right-hand side of this equation, we omitted the contributions to the process of evolution of the dislocation density from dislocation sources in the bulk of the crystal, as well as from the multiplication and immobilization of dislocations on obstacles of a nondeformation origin, because the crystals are assumed to be sufficiently pure.

In the case of coarse-sized crystals, the first two terms in the right-hand side of Eqn (21) make an insignificant contribution to the process of the evolution of the dislocation density. Omitting them, we obtain the well-known equation $d\rho/d\gamma = k_f\rho^{1/2} - k_a\rho$; solving it and using the Taylor relation $\tau = \alpha\mu b\rho^{1/2}$, we obtain the dependence of the flow stress τ on the deformation γ and of the coefficient of strain hardening $\theta = d\tau/d\gamma$ on the stress τ at the second and third stages of the curves of strain hardening of fcc crystals:

$$\tau = \tau_3\left[1 - \exp\left(-\frac{\gamma}{\gamma_3}\right)\right], \tag{22a}$$

$$\theta = \theta_{II}\left(1 - \frac{\tau}{\tau_3}\right), \tag{22b}$$

where $\tau_3 = \alpha\mu b\rho_3^{1/2}$ and $\rho_3 = (k_f/k_a)^2$ are the flow stress and the dislocation density at the end of the third stage of strain hardening, $\theta_{II} = (1/2)\,\alpha(bk_f)\,\mu \approx (2-2.5)\times 10^{-3}\mu$ is the strain hardening coefficient at the second (linear) stage of strain hardening of a massive crystal [135], and $\gamma_3 = 2/k_a$ is the characteristic length of the third stage.

Using the full equation (21), we consider the evolution of the curves of strain hardening $\tau(\gamma)$ and of their parameters under a change in a wide range, from 1 mm to 100 nm, in the transverse dimensions of the crystal. For this, we use the relation $\tau(d\tau/d\gamma) = (1/2)(\alpha\mu b)^2(d\rho/d\gamma)$, which follows from the Taylor law $\tau = \alpha\mu b\rho^{1/2}$. It relates the coefficient of strain hardening of the crystal ($\theta = d\tau/d\gamma \sim d\rho/d\gamma$) to the dislocation-kinetics processes that develop in a crystal subjected to deformation (21). Substituting the dislocation density specified by the Taylor law $\rho = (\tau/\alpha\mu b)^2$ in Eqn (21), we obtain the dependence of the SH coefficient on the dimensionless flow stress $\tau_* = \tau/\tau_3$ [58, 127]:

$$\frac{d\tau}{d\gamma} = \theta(\tau_*) = \theta_{II}\left(\frac{Q_0}{\tau_*^3} - \frac{Q_1}{\tau_*} + 1 - \tau_*\right), \tag{23a}$$

$$Q_0 = \frac{\eta_S}{bD^3k_f\rho_3^{3/2}}\,,\quad Q_1 = \frac{m_e}{bDk_f\rho_3^{1/2}}\,. \tag{23b}$$

The parameters Q_0 and Q_1, as we show below, determine the appearance of the zeroth and first stages in the SH curve of the crystal. The zeroth stage, or the stage of microdeformation, is related to the operation of dislocation sources. The first (quasilinear) stage, or the easy-slip stage, is transient between the zeroth and second (linear) stages of strain hardening. The first stage is determined by the third term in parentheses in Eqn (23a); the last, fourth term controls the third (quasiparabolic) stage of strain hardening — the stage of dynamic recovery. The SH coefficient at these last two stages corresponds to the Voce empirical relation in Eqn (22b).

Parameters (23b) can be written in a more compact and physically clearer form as [58]

$$Q_0 = \left(\frac{D_S}{D}\right)^3,\quad Q_1 = \omega\left(\frac{D_S}{D}\right), \tag{23c}$$

where

$$D_S = \left(\frac{\eta_S}{bk_f}\right)^{1/3}\rho_3^{-1/2}\,,\quad \omega = \frac{m_e}{(bk_f)^{2/3}\eta_S^{1/3}}\,.$$

The parameter combination D_S specifies the characteristic dimensions of the transverse section of the crystal at which the flow stress becomes sensitive to the size factor; the combination ω determines the relation (competition) between the processes of generation of dislocations from the surface sources ($\eta_S = 2/\delta_S^3$), multiplication of dislocations on forest dislocations ($bk_f = \delta_f \approx 10^{-2}$), and escape of dislocations from the crystal through its surface ($m_e = \sin\varphi$). At $\varphi = 0$, the dislocations cannot escape from the crystal through its surface; at $\varphi = \pi/2$, their path to the surface is equal to the transverse dimension D of the crystal.

Integrating Eqn (23a) and taking into account that $\tau_3/\theta_2 = \gamma_3 = 2/k_a$, we obtain the dependence of the reduced flow stress τ_* on the reduced shear strain γ/γ_3 in implicit form:

$$\int_0^{\tau_*} \frac{d\tau_*}{Q_0\tau_*^{-3} - Q_1\tau_*^{-1} + 1 - \tau_*} = \frac{\gamma}{\gamma_3} . \tag{24}$$

Equations (23) and (24) are used below for a quantitative analysis of the effect of the transverse dimensions of the crystal on the type and parameters of its strain hardening curve.

We first consider the effect of the crystal dimension D on the type of the dependence of the dimensionless SH coefficient $\theta/\theta_{\rm II}$ on the stress $\tau_* = \tau/\tau_3$ according to Eqn (23). Figure 17a displays the corresponding dependences (curves *1–5*) and Table 1 gives the relative dimensions of crystals $D/D_{\rm S}$ and the values of the parameter ω that were used for constructing these dependences. It follows that in the relatively coarse-sized crystal, with $D \gg D_{\rm S}$ (curve *1*), the SH coefficient varies with the stress according to Voce equation (22b). At substantially smaller transverse sections of the crystal (curve *2*), a zeroth stage (stage of microdeformation) appears in the dependence of θ on τ, with an SH coefficient substantially exceeding the coefficient $\theta_{\rm II}$ corresponding to the second stage of strain hardening of a massive crystal. Another specific feature of curve *2* is the appearance of a minimum and a maximum, which are related to the first (quasilinear) and second (linear) stages of strain hardening. An analysis shows that these extrema arise at the respective stresses τ_1 and τ_2 such that

$$\frac{\tau_{1,2}}{\tau_3} = \left(\frac{\omega}{2D_*}\right)^{1/2}\left[1 \mp \sqrt{1 - G(D_*)}\right]^{1/2} , \tag{25a}$$

$$G(D_*) = \frac{12}{\omega^2 D_*} , \quad D_* = \frac{D}{D_{\rm S}} . \tag{25b}$$

Figure 17b displays the strain hardening curve of the crystal in the coordinates $(\tau/\tau_3, \gamma_*)$, where $\gamma_* = \gamma/\gamma_3 + \gamma_{\rm el}/\gamma_3$, $\gamma_{\rm el}/\gamma_3 = (\tau/\tau_3)/K_*$ is the reduced elastic deformation, $K_* = 8$, $K_* = (K/\tau_3)\,\gamma_3 = K/\theta_{\rm II}$ and K is the coefficient of rigidity of the sample–loading-device system. The curve was obtained by integrating Eqn (24) with the SH coefficient corresponding to curve *2* in Fig. 17a. The dashed lines show the stresses τ_1 and τ_2. The stress τ_1 corresponds to the inflection point at the first stage of SH; the stress τ_2 determines the maximum value of the strain hardening coefficient at the second stage, after which the coefficient begins decreasing in the third stage (dynamic recovery stage).

Thus, as a result of thinning of the crystal, the two-stage SH curve of a massive crystal transforms into a five-stage curve (Fig. 17b). Substituting the stresses $\tau_1(D_*)$ and $\tau_2(D_*)$ in Eqn (23a), we obtain the dependences of the SH coefficients at the first and second stages on the crystal dimension $D_* = D/D_{\rm S}$:

$$\theta_1(D_*) = \theta_{\rm II}\left(\frac{1}{D_*^3\tau_{*1}^3} - \frac{\omega}{D_*\tau_{*1}} + 1 - \tau_{*1}\right) , \tag{26a}$$

$$\theta_2(D_*) = \theta_{\rm II}\left(\frac{1}{D_*^3\tau_{*2}^3} - \frac{\omega}{D_*\tau_{*2}} + 1 - \tau_{*2}\right) , \tag{26b}$$

where we introduce the brief notation $\tau_{*1} = \tau_1(D_*)/\tau_3$ and $\tau_{*2} = \tau_2(D_*)/\tau_3$. The correspondence of relations (26) to the experimental data is illustrated in Fig. 12, where curves *1* and *2* demonstrate these dependences at the parameter values $\theta_{\rm II} = 200$ MPa, $\omega = 1.75$, and $D_{\rm S} = 2.5$ μm.

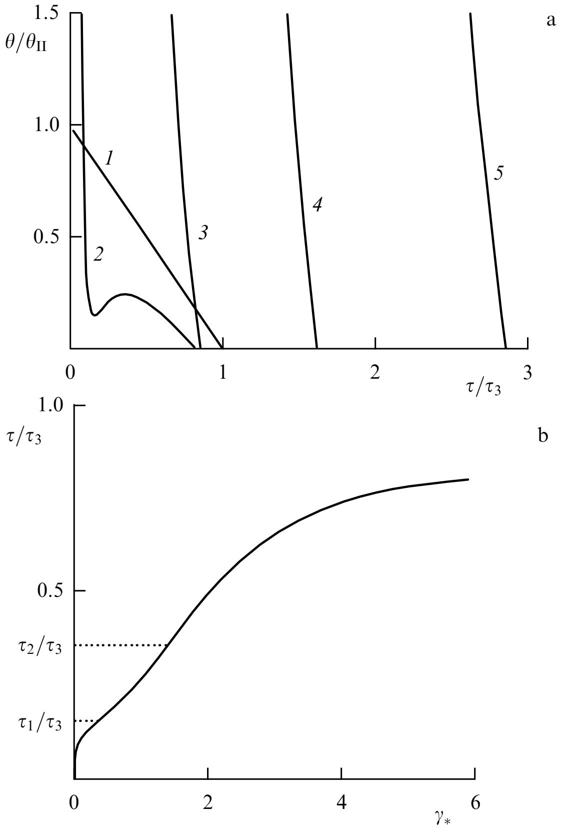

Figure 17. (a) Dependence of the dimensionless strain hardening coefficient $\theta/\theta_{\rm II}$ on the reduced flow stress $\tau_* = \tau/\tau_3$ according to (23) at various relative transverse dimensions of the crystals $D/D_{\rm S}$ (see Table 1) and (b) strain-hardening curve of the crystal in $(\tau/\tau_3, \gamma_*)$ coordinates according to Eqn (24) and relations (23).

Table 1. Relative dimensions of crystals $D/D_{\rm S}$ and the values of the parameters ω and G used for constructing curves *1–5* in Figs 17a and 18.

Curve no.	$D/D_{\rm S}$	ω	G
1	10^3	1.5	5.3×10^{-3}
2	10	1.5	0.53
3	1	1.5	5.3
4	0.4	2.0	7.5
5	0.2	2.0	15.0

It can be seen from relations (25) and Table 1 that as the crystal size decreases, an instant comes when the parameter G becomes greater than unity. At the critical value $G = 1$ corresponding to the critical crystal size $D_{\rm c}$, the stresses τ_1 and τ_2 and the coefficients θ_1 and θ_2 are equal to one another. In this case, according to (25) and (26), we have

$$D_{\rm c} = \frac{12}{\omega^2} D_{\rm S} , \quad \tau_1 = \tau_2 = \left(\frac{\omega^3}{24}\right)^{1/2} \tau_3 , \\ \theta_1 = \theta_2 = \theta_{\rm II}\left[1 - \left(\frac{2}{3}\,\omega\right)^{3/2}\right] . \tag{27}$$

In the above-considered case of copper crystals, the critical size $D_{\rm c} \approx 4D_{\rm S}$ is equal to 10 μm, which is in good agreement with the data given in Fig. 12.

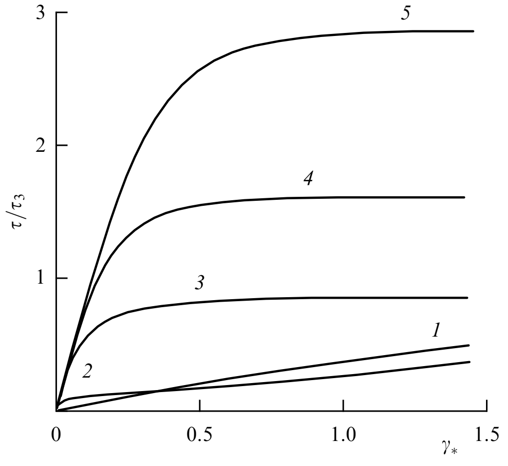

Figure 18. Strain-hardening curves of crystals in $(\tau/\tau_3,\ \gamma_*)$ coordinates according to Eqn (24) and relations (23) at the relative dimensions D/D_{S} and values of the parameter ω given in Table 1.

At crystal sizes $D < D_{\mathrm{c}}$, the character of the dependences of the SH coefficient on the stress τ (Fig. 17a) and the shape of the SH curves $\tau(\gamma)$ (Fig. 18) obtained by integrating Eqn (24) changes substantially. These dependences (curves *3*–*5*) contain only the stage of microdeformation (zeroth stage), which terminates after reaching an equilibrium between the rate of generation of dislocations from sources and the escape of dislocations from the crystal. Neglecting the last two terms in the right-hand side of Eqn (21), we obtain the equation

$$\rho\,\frac{\mathrm{d}\rho}{\mathrm{d}\gamma} = \frac{\eta_{\mathrm{S}}}{bD^3} - \left(\frac{m_{\mathrm{e}}}{bD}\right)\rho\,. \tag{28}$$

It follows from Eqn (28) that the dynamic equilibrium between the emission of dislocations from sources and their escape through the crystal surface sets in at the dislocation density $\rho_{\mathrm{D}} = \eta_{\mathrm{S}}/m_{\mathrm{e}}D^2$. After removal of the loading, this density, according to the equation $\mathrm{d}\rho/\mathrm{d}t = -(m_{\mathrm{e}}u/D)\,\rho$, relaxes from the crystal under the image forces in accordance with the exponential law $\rho(t) = \rho_{\mathrm{D}}\exp(-t/t_{\mathrm{D}})$, where t is time, u is the dislocation velocity, and $t_{\mathrm{D}} = D/m_{\mathrm{e}}u$ is the characteristic relaxation time, which becomes smaller as the crystal becomes thinner.

In the case of crystals with dimensions $D \ll D_{\mathrm{c}}$, we omit the last two terms in Eqn (24) in the denominator of the integrand to obtain the (implicit) dependence of the reduced flow stress $\tau_* = \tau/\tau_3$ on the deformation γ and the dimensionless crystal thickness $D_* = D/D_{\mathrm{S}}$:

$$\ln\frac{1}{1-\omega D_*^2\tau_*^2} - \omega D_*^2\tau_*^2 = \frac{\gamma}{\gamma_{\mathrm{D}}}\,, \tag{29}$$

where $\gamma_{\mathrm{D}} = \gamma_3/2\omega^2 D_*$. According to Eqn (29), at the initial stage of deformation, when the generation of dislocations from a source is predominant and the condition $\omega D_*^2\tau_*^2 \ll 1$ is satisfied, the dependence of the stress τ_* on γ is $\tau_* \approx (4\gamma/\gamma_3 D_*^3)^{1/4} \sim D^{-3/4}$. On the other hand, at stresses $\omega D_*^2\tau_*^2 \approx 1$, Eqn (29) implies the $\tau_*(\gamma)$ dependence

$$\tau_* = \left(\frac{1}{\omega D_*^2}\right)^{1/2}\left[1 - A\exp\left(-\frac{\gamma}{\gamma_{\mathrm{D}}}\right)\right]^{1/2}, \quad A = e^{-1}. \tag{30}$$

It follows from expression (30) that at $\gamma \gg \gamma_{\mathrm{D}}$, the flow stress tends to an equilibrium value $\tau_{\mathrm{fl}} = (1/\omega D_*^2)^{1/2}\tau_3 \sim 1/D$, which depends on the transverse size of the crystal. The parameter $\gamma_{\mathrm{D}} \sim 1/D$ determines the characteristic deformation magnitude required for reaching a dynamic equilibrium between the emission of dislocations from sources and their escape from the crystal. We note that the smaller the relative size of the crystal is, $D \ll D_{\mathrm{S}}$, the closer relations (29) and (30) are quantitatively to each other and to the result of the integration of the full equation (24).

In dimensional form, in accordance with (29) and (30), we therefore have the following dependences of the yield stress τ_{y} (at $\varepsilon_{\mathrm{y}} = m_{\mathrm{Sm}}\gamma_{\mathrm{y}} \approx 0.2\%$), the deformation γ_{D}, and the equilibrium flow stress τ_{fl} on the transverse dimension of the crystal D:

$$\tau_{\mathrm{y}} = k_{\mathrm{y}}\left(\frac{b}{D}\right)^{3/4}\mu\,, \quad k_{\mathrm{y}} = \alpha(2m_{\mathrm{Sm}}\varepsilon_{\mathrm{y}}\eta_{\mathrm{S}})^{1/4}\,, \tag{31a}$$

$$\gamma_{\mathrm{D}} = k_{\mathrm{D}}\left(\frac{b}{D}\right), \quad k_{\mathrm{D}} = \frac{\eta_{\mathrm{S}}}{m_{\mathrm{e}}^2}\,, \tag{31b}$$

$$\tau_{\mathrm{fl}} = k_{\mathrm{fl}}\left(\frac{b}{D}\right)\mu\,, \quad k_{\mathrm{fl}} = \alpha\left(\frac{\eta_{\mathrm{S}}}{m_{\mathrm{e}}}\right)^{1/2}. \tag{31c}$$

It follows from Eqn (31b) that the smaller the crystal dimension is, the greater the deformation γ_{D} necessary to achieve equilibrium between the emission of dislocations from sources and their escape from the crystal. This is confirmed experimentally (Fig. 15a, curves *4*–*6*) [4, 139].

In accordance with relation (31b), under deformations of 10–15%, the dependence $\tau_{\mathrm{fl}} \sim D^{-1}$ of the flow stress on the crystal dimension was revealed in crystals of Ni (Fig. 15b, curve *2*), Au [142], and Ag [157] (Table 2). The data in Table 2 show that the coefficient k_{fl} for various metals changes in the narrow range $k_{\mathrm{fl}} \approx 11-13$; on average, therefore, relation (31c) for fcc metals has a universal value $k_{\mathrm{fl}} \approx 12$, $n = 1$.

At the initial (zeroth) stage of deformation, $\tau_{\mathrm{y}} \sim D^{-n}$ dependences with $n = 0.6-0.7$ have been found in many studies. For example, Table 2 gives corresponding data for crystals of Au [143], Ni [138, 139], and LiF [169]. The authors of [145] suggest a universal relation for the empirical dependences of this type for fcc metals, $\tau_{\mathrm{y}} = k_{\mathrm{y}}(b/D)^n\mu$, where $n = 0.67$ and $k_{\mathrm{y}} = 0.7$. The exponent n in this expression is 10% less than that in Eqn (31a).

Of great interest are quantitative estimates (according to the data in Table 2) of the parameter δ_{S}, the critical length $L_{\mathrm{FR}} = \delta_{\mathrm{S}}D$, and the stress for activation of an FR source $\tau_{\mathrm{FR}} = \mu b/L_{\mathrm{FR}}$ in (19). For the 'universal' value $k_{\mathrm{fl}} = 12$ at $\alpha = 0.5$ and $m_{\mathrm{e}} = \sin\varphi = 1/\sqrt{2}$, we find, according to (31c), that $\eta_{\mathrm{S}} = 407$, $\delta_{\mathrm{S}} = 0.17$, and $\tau_{\mathrm{FR}} \approx 6(\mu b/D)$. This stress is half the flow stress given by (31c), but is six times greater than the minimum possible stress for the activation of an FR source in a nanocrystal, $\mu b/D$. Substituting the above-obtained values of η_{S} and $\alpha = 0.5$ in (31a), at $m_{\mathrm{Sm}} = 0.5$ and the universal value of the coefficient $k_{\mathrm{y}} = 0.7$ [145], we then obtain a deformation $\varepsilon_{\mathrm{y}} \approx 1\%$ at which stresses of the onset of plastic deformation of micro- and nanocrystals are usually determined.

Thus, in terms of the dislocation-kinetics approach with the above assumptions, the mechanisms of dislocation starvation and exhaustion of strain hardening, widely discussed in the literature, can be explained and qualitatively verified as characteristic features of plastic deformation of micro- and nanosized crystals.

Table 2. Experimental values of the coefficients k_y and k_{fl} and the exponents n for micro- and nanocrystals of various metals and LiF.

Crystal	D, μm	n	k_y	k_{fl}	b, nm	μ, GPa	References
Au	0.1 – 10	0.6	0.44	—	0.28	27.8	[143]
Au	0.2 – 10	1.06	—	12.5	—	—	[142, 148]
Ni	1.0 – 20	0.67	0.57	—	0.25	75.0	[138, 139]
Ni	0.2 – 20	1.0	—	13.3	—	—	[139]
Ag	0.1 – 1.0	1.0	—	11.0	0.25	25.5	[157]
Cu	5.0 – 20	1.0	—	13.0	0.26	48.0	[124]
LiF	1.0 – 20	0.74	3.6	—	0.28	65.8	[169]

As regards the plastic deformation of defect-free crystals [13, 14, 124, 163, 187, 188] that develops in accordance with a catastrophic scenario (see Fig. 14), the order-of-magnitude higher values $k_y \approx 100-300$ in relations (17) are related to a low density of subsurface dislocation sources in defect-free crystals and, correspondingly, their strong sensitivity to the size factor. The absence of dislocations in them is explained by the high perfection of the surface of crystals, which is related to the technology of their production from the gas phase (in the form of whiskers) or as a result of high annealing (Mo [159, 160]). The catastrophic character of the development of plastic deformation in such crystals is related to a rapid process of generation of dislocations and the formation of a Luders front [187, 188]. The increase in the density of surface and bulk dislocation sources as a result of a preliminary deformation of nanocrystals is accompanied by a decrease in their strength and by the loss of their sensitivity to the size factor [159].

We note in the conclusion of this section that the quantitative analysis in terms of the dislocation-kinetics approach does not cover only the above-mentioned catastrophic character of deformation of defect-free nano- and microcrystals and the compressive and tensile strength of nanosized samples of NC metals with the ratio of the size of samples and the size of grains $D/d < 30$, in which case a thinning of a nanocrystalline sample leads to a decrease in strength rather than to its increase [188]. Among the problems that have not been considered in terms of the above approach, the high sensitivity of the micro- and nanosized tensile samples to neck formation should also be mentioned [137, 189].

3.2 Plastic deformation gradient and geometrically necessary (GN) dislocations

As was already noted in the Introduction, for samples with the transverse size 1–10 μm, inhomogeneous (on a micron level) deformations by torsion [20], bending [21, 22], and micro- and nanoindentation [23–25] lead to an enhanced resistance to plastic deformation compared to its homogeneous distribution in uniaxially stretched or compressed samples of the same cross section. The observed size effect of additional strengthening is usually ascribed to the generation of GN dislocations (with the density $\rho_{\text{gn}} = b^{-1}(\mathrm{d}\gamma/\mathrm{d}x)$) in the process of inhomogeneous deformation because of the existence of a plastic deformation gradient (PDG) $\mathrm{d}\gamma/\mathrm{d}x$ in the sample cross section. According to the Ashby hypothesis [190] and the Taylor formula, we can then express the flow stress as $\tau = \alpha\mu b\sqrt{\rho_{\text{S}} + \rho_{\text{gn}}}$, where ρ_{S} is the density of randomly stored (statistically distributed) dislocations arising under homogeneous deformation.

3.2.1 Plastic deformation gradient. At present, in the theoretical analysis of the size factor, a phenomenological approach is mainly used, based on the classical theory of plasticity with the PDG taken into account [20–23]. According to this approach, the above Taylor–Ashby relation can be represented as $\tau = \tau_{\text{S}}\sqrt{1 + l_{\text{S}}\chi}$, where $\chi = \mathrm{d}\gamma/\mathrm{d}x$ is the deformation gradient, l_{S} is a characteristic length depending on the structural factors and the degree of plastic deformation γ, and $\tau_{\text{S}} = \alpha\mu b\rho_{\text{S}}^{1/2}$ is the flow stress in the absence of a deformation gradient. At the initial stage of deformation, at the yield-stress level, we have $\tau_{\text{S}} = \tau_0$ and $l_{\text{S}} = l_0 = (\alpha\mu/\tau_0)^2 b$; as a result, we obtain the relation $\tau/\tau_0 = \sqrt{1 + l_0\chi}$. This relation was used in [23] for an analysis of the dependence of the microhardness H of Cu and Ag single crystals on the depth of indentation in the range of depths $h = 0.15 - 2$ μm. Taking into account that $H \approx 3\sigma$, where $\sigma = \tau/m_{\text{Sm}}$ is the compressive stress, and that $\chi = \delta/h$, where δ is a coefficient depending on the geometry of the indenter tip [23], we obtain the following relation for the microhardness:

$$\frac{H}{H_0} = \sqrt{1 + \frac{h_*}{h}}, \quad h_* = \delta l_0 \,. \tag{32}$$

A comparison of expressions (32) with the experimental data shows good agreement at the characteristic parameter values $h_* = 0.5 - 1.5$ μm and $H_0 = 0.3 - 0.8$ GPa [23]. As was noted in a recent review of mechanistic models of the PDG effect on the flow stress of samples deformed by bending [22], this correspondence is conceptually not fully consistent with the Ashby assumption that $\tau \sim \sqrt{\rho_{\text{S}} + \rho_{\text{gn}}}$. This circumstance was also noted in [191] from the standpoint of the dislocation mechanism of plastic deformation.

Recent experiments on the plastic bending of thin single-crystal samples of copper [192] and nanocrystalline samples of nickel [193] in a wider range of transverse dimensions and deformations than in [20, 21] allowed concluding that the situation with the PDG effect on the strength is more complex and ambiguous than was expected previously.

For example, estimates of the density of GN dislocations arising during cantilever bending of copper single crystals of the thickness $D = 1 - 7.5$ μm showed [192] that their contribution to the size effect does nor exceed 10% at the crystal thickness 1 μm and that the remaining part of the increase in the strength (Fig. 19a) is related to some other factors. Figure 19b displays the results of processing the data given in

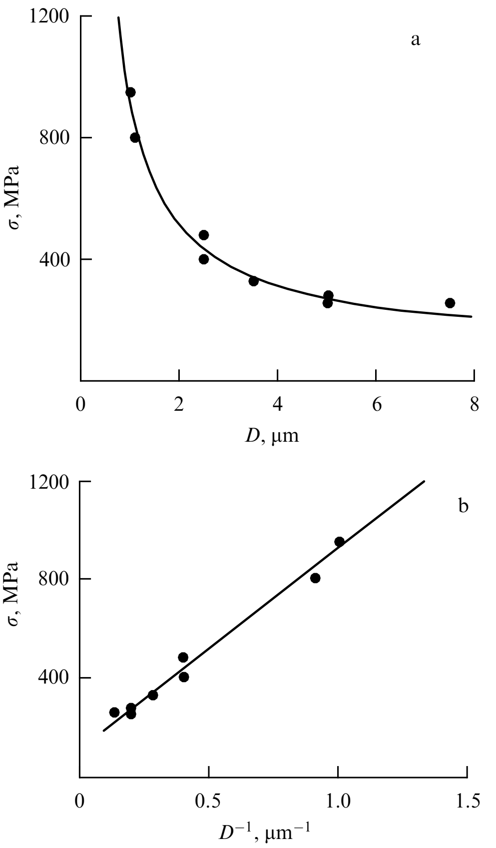

Figure 19. Dependence of the flow stress σ under cantilever bending of single-crystal samples of copper [192] on (a) the sample thickness D and (b) its inverse value D^{-1}.

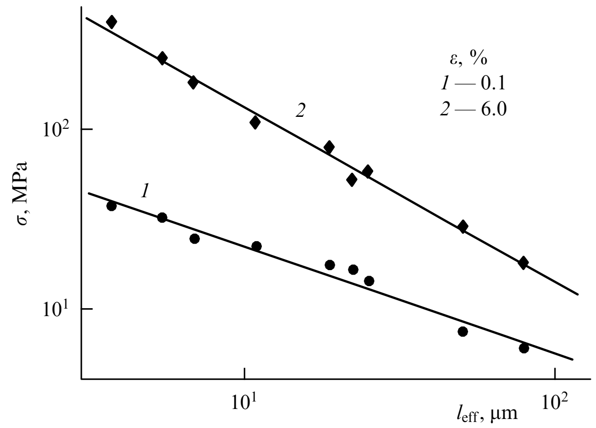

Figure 20. Dependence of the flow stresses under bending of microcrystalline samples of nickel [193] on the effective dimension $l_{eff} = (d^{-1} + D^{-1})^{-1}$ in two stages of deformation ε.

Fig. 19a in the (σ, $1/D$) coordinates, where σ is the average tensile (compressive) stress over the crystal cross section calculated from the magnitude of the bending moment corresponding to the developed plastic flow of the sample. It follows from Fig. 19b that the flow stress obeys relations such as (18) and (31), $\sigma = \sigma_0 + k'_{fl}(\mu b/D)$ with $\sigma_0 = 120$ MPa and $k'_{fl} \approx 70$. The coefficient k'_{fl} for the tensile stress σ is related to the coefficient k_{fl} for the shear stress τ as $k'_{fl} = (2/m_{Sm})\, k_{fl}$, where the coefficient 2 takes into account that the tension (compression) is applied to only half the crystal thickness. At the Schmid factor values $m_{Sm} = 0.3-0.4$, we obtain an estimate $k_{fl} \approx 11-14$ for copper, which is close to the values of this coefficient for various fcc metals in the absence of a PDG (see Table 2). This means that in the experiment under consideration, the predominant factor that determines the size effect is not the PDG but the crystal thickness itself, as well as the existence of dislocation sources in the crystal, as is the case in a homogeneous distribution of stresses over the cross section of a thin crystal (see Section 3.1).

An unusual result was obtained with the plastic bending of microcrystalline Ni samples when varying the grain size and sample thickness in wide ranges ($d = 7-300$ μm and $D = 10-125$ μm) [193]. It turned out that the flow stresses related to the sample bending, irrespective of the degree of plastic deformation, are determined by the effective dimension $l_{eff} = (1/d + 1/D)^{-1}$. Curves *1* and *2* in Fig. 20 demonstrate these results for two degrees of bending deformation, $\varepsilon = 0.1$ and 6%. Assuming that the deformation of 0.1% corresponds to the yield stress of the sample σ_y and the deformation of 6% to the developed plastic deformation, the data shown in Fig. 20 can be represented in the form of relations (18) and (31),

$$\sigma_y = k'_y \left(\frac{b}{l_{eff}}\right)^{0.6} \mu\,, \quad \sigma_{fl} = k'_{fl} \left(\frac{b}{l_{eff}}\right) \mu\,, \tag{33}$$

with the coefficients k'_y and k'_{fl} respectively equal to 0.17 and 64.5. We note that the value of k'_{fl} for the microcrystalline Ni is close to that for single-crystal copper ($k'_{fl} = 70$) considered above. Taking the 'composite' character of the effective size l_{eff} into account, the relation between the coefficient k_{fl} for the shear stress τ_{fl} and the coefficient k'_{fl} for the tensile (compressive) stress σ_{fl} in (33) can be written in the form of a combination of the Schmid and Taylor coefficients: $k'_{fl} = \left[(2/m_{Sm} + m_T)/2\right] k_{fl}$. At $m_{Sm} \approx 0.3-0.5$ and $m_T = 3.05$, we obtain $k_{fl} \approx 10-14$. This estimate virtually coincides with the value of this coefficient for microsized samples of single-crystal nickel deformed under uniaxial compression (Table 2). Just as in the case of bending of copper single crystals, this circumstance can serve as an argument in favor of the idea that the factor that determines the size effect is here, as in the preceding case, the crystal thickness by itself, rather than the plastic deformation gradient.

As regards the first relation in (33), the exponent equal to 0.66 is also characteristic of the flow stresses of micro- and nanosized crystals at the degrees of homogeneous compressive deformation that do not exceed 1–3% (see Section 3.1.1, Fig. 16). On the other hand, it is also close to the exponent 0.5 in the HP relation $\sigma = K_{HP} d^{-1/2}$ for polycrystals such as the samples of microcrystalline nickel with the grain size $d \leqslant D$. In [193], results are also presented that indicate that at the initial stage of deformation (at the yield stress), the flow stresses of nickel can be represented as an additive contribution of two size factors:

$$\sigma_y = K_{HP} d^{-1/2} + K_y \left(\frac{b}{D}\right) \mu\,, \tag{34}$$

where $K_{HP} = 0.33$ MPa m$^{1/2}$, irrespective of the sample thickness D, and $K_y = 23$. The available experimental data cannot help in choosing between relations (33) and (34). We also note that if there is a correlation between the grain sizes and transverse dimensions of crystals, e.g., $d \sim D^q$ (where $q > 0$), which is related to the technology of crystal preparation, as is the case with the bending of samples of microcrystalline copper [194], then, simultaneously with the HP relation $\sigma_{\rm y} = K_{\rm HP} d^{-1/2}$ with the coefficient $K_{\rm HP} = 0.2$ MPa m$^{1/2}$, the dependence $\sigma_{\rm y} = K_{\rm y}(b/D)\,\mu$ appears with the coefficient $K_{\rm y} \approx 5$ caused by this correlation.

The ambiguity related to the origin of the size effect in the presence of a PDG and the contribution to it from the GN dislocations were discussed in detail in [191, 195, 196]. The authors of these studies arrived at the conclusion that the contribution from the GN dislocations to the size effect can be revealed only if the density of GN dislocations $\rho_{\rm gn}$ in the Taylor–Ashby formula $\tau \sim \sqrt{\rho_{\rm S} + \rho_{\rm gn}}$ substantially exceeds the density of statistical dislocations $\rho_{\rm S}$. Otherwise, the separate contributions of these densities cannot be distinguished because of their mutual dependence. Just such a situation occurs in the experiments in [192] and [193].

3.2.2 Geometrically necessary dislocations. Situations can exist (and are observed in experiments) where the density of GN dislocations exceeds the density of statistical dislocations, for example, when kink bands arise in a bulk single crystal or in a polycrystal, as a result of local bending in the form of two walls of GN dislocations of the opposite sense (Fig. 21), which misorient the crystal between the walls by an angle ω from $1° - 2°$ to $30° - 60°$ with the spacing Λ between the walls in the range from 1 μm to 1 mm [197–200]. Another example is given by the phenomenon of so-called dynamic polygonization, which is observed upon the bending of a massive crystal and leads to the formation of a regular structure of walls of GN dislocations of the same sense perpendicular to the slip plane and plastically adapting the bending of the crystal [198, 201–203].

The mechanism of the formation of kink bands was considered from the standpoint dislocation kinetics in [200]. The solution of the kinetic equations for the density of dislocations of different signs, ρ^+ and ρ^-, is given by the following dependences on the coordinate x along the slip plane of dislocations, the shear deformation γ, and time t:

$$\rho^{\pm}(x, \gamma, t) = \rho^{\pm}_{\rm m}\,\frac{1 - \exp(-k_{\rm a}\gamma)}{\cosh^2\big((x \pm Ut)/\Lambda_{\pm}\big)}\,, \tag{35a}$$

$$\rho^{\pm}_{\rm m} = \frac{3(k_{\rm m} - k_{\rm im})_{\pm}}{2k_{\rm a}}\,, \quad \Lambda_{\pm} = 2\left[\frac{(\xi_x - 1)\,\lambda_x}{b(k_{\rm m} - k_{\rm im})_{\pm}}\right]^{1/2}. \tag{35b}$$

Here, $k_{\rm m} = 1/b\lambda_{\rm m}$ and $k_{\rm im} = 1/b\lambda_{\rm im}$ are the coefficients of multiplication and immobilization of dislocations on obstacles of nondeformation origin ($k_{\rm m} > k_{\rm im}$), $\lambda_{\rm m}$ and $\lambda_{\rm im}$ are the corresponding paths of dislocations [56, 109], $k_{\rm a}$ is the coefficient of annihilation of screw segments of dislocation loops [56, 204], λ_x is the characteristic distance of diffusion of dislocations along the x axis, $\xi_x > 1$ is the parameter corresponding to the appearance of a Turing instability and dislocation clustering in a dislocation ensemble [56, 109], and U is the velocity of motion of dislocation walls.

The authors of [205] note that a nucleus of a kink band arises as a result of the spatial separation (polarization) of two dislocation walls of different signs. Figure 21a displays the distribution [according to Eqn (35a)] of dislocation densities ρ^+ and ρ^- at the initial instant $t = 0$ at $\gamma \gg 1/k_{\rm a}$, the ratio of densities $\rho^+_{\rm m}/\rho^-_{\rm m} = 1.4$, and the ratio of the wall widths $\Lambda_+/\Lambda_- = (\rho^-_{\rm m}/\rho^+_{\rm m})^{1/2} \approx 0.85$. Figure 21b demonstrates the result of the motion of walls in the form of two solitons moving in opposite directions with the formation of a band of a lattice reorientation between them, where $z = x - Ut$. The motion (drift) of a low-angle tilt boundary along a Zn crystal during its cantilever bending under the action of a constant load suspended at the free end was observed in [206].

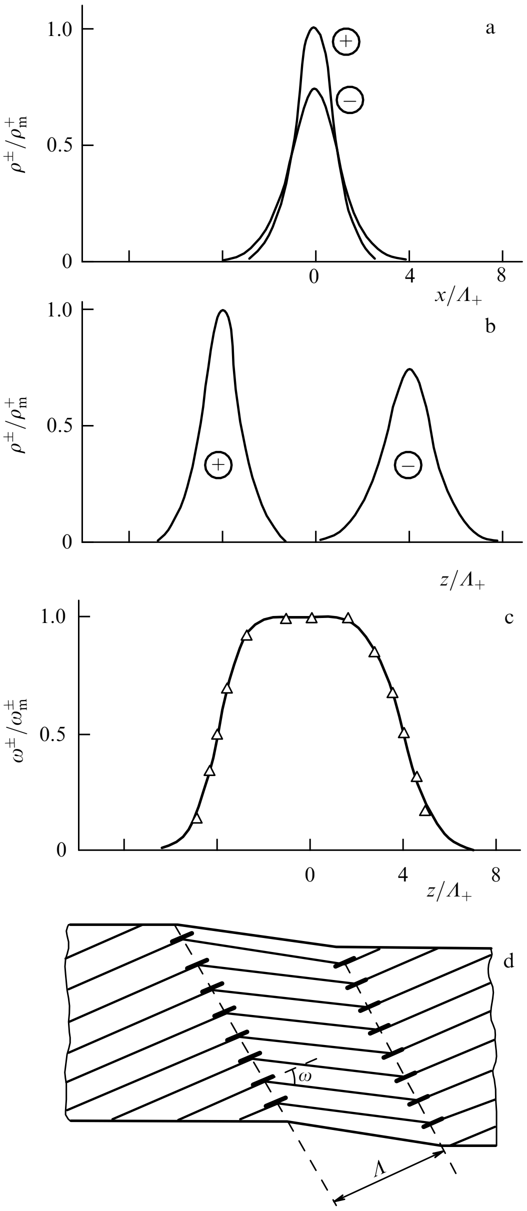

Figure 21. (a–c) Dislocation-kinetics mechanism of the formation of a kink band according to Eqns (35) and (36); and (d) diagram of the kink band. The experimental points correspond to the distribution of the rotation angles in the kink band in an aluminum crystal [199].

Figure 21c demonstrates the results of the calculations of the misorientation angles $\omega^{\pm}$ of the walls:

$$\omega^{\pm}(x, \gamma, t) = b\int_{-\infty}^{x} \rho^{\pm}(x, \gamma, t)\,{\rm d}x$$
$$= \omega^{\pm}_{\rm m}\big[1 - \exp(-k_{\rm a}\gamma)\big]\left[1 \pm \tanh\left(\frac{x \pm Ut}{\Lambda_{\pm}}\right)\right], \tag{36}$$

where $\omega^{\pm}_{\rm m} = b\rho^{\pm}_{\rm m}\Lambda_{\pm}$ and $2Ut = \Lambda$ is the width of the band (see the diagram in Fig. 21d). The experimental points in Fig. 21c show the result of measuring the rotation angles in a kink band in an aluminum crystal at the wall widths $\Lambda_+ = 11$ μm and $\Lambda_- = 15$ μm [199]. These results show that in contrast to the traditional representation of a kink

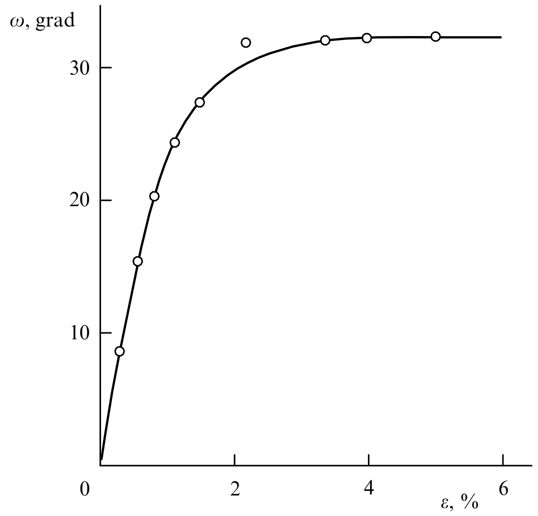

Figure 22. Dependence of the angle of lattice rotation in the kink band in a Zn crystal on the magnitude of deformation [205]. The curve is constructed in accordance with Eqn (36) at $x \pm Ut = 0$, $\omega_m = 33°$, and $m_{Sm}k_a = 150$.

band (Fig. 21d), the real walls of the bands have a significant width comparable to the dislocation path λ_m and λ_{im} and a complex structure with the lattice rotation angle ω depending on both the coordinate and the deformation γ. As an illustration, Fig. 22 shows the dependence of the rotation angle in the kink band of a Zn crystal [205] on the tensile deformation $\varepsilon = m_{Sm}\gamma$. The curve shown in this figure demonstrates the growth of the maximum rotation angle in the band in accordance with (36), $\omega_{\max}(\varepsilon) = \omega_m\left[1-\exp\left(-m_{Sm}k_a\varepsilon\right)\right]$, as a result of an increase in the density of GN dislocations in its walls.

The kink bands and the GN dislocations arise at the sites of concentration of dislocations and difficulty of slip deformation. As was noted in [191, 196], such a situation occurs at the boundaries of dislocation cells upon the formation of a cellular dislocation structure. As a result, under large plastic deformations, a blocked dislocation structure is formed in the metal, consisting of crystalline fragments (blocks) 100–400 nm in size with the angles of misorientation of the crystal lattice from 1° to 45° [7–9]. This fragmentation under equal-channel angular pressing [7, 207], rolling [196, 208], and high-pressure torsion [9] is the basis of modern methods of production of nanocrystalline metals and alloys.

From the standpoint of dislocation kinetics, the mechanism of the formation of a blocked dislocation structure and fragmentation of metallic materials has been considered in [209–212]. As is well known, at moderate degrees of deformation in the material, first, a weakly misoriented ($1°-2°$) cellular dislocation structure is formed [213–216]. According to [56, 217, 218], the distribution of the density of statistical dislocations ρ_S in this structure is given by

$$\rho_S(x,\varepsilon) = \frac{\rho_{\max}(\varepsilon)}{\left[1+\left(f(\varepsilon)-1\right)\sin^2(\pi x/\Lambda)\right]^2}\,, \qquad (37)$$

where $\rho_{\max}(\varepsilon) = \rho_m v^2(\varepsilon)$ is the density of dislocations at the center of dislocation cells (Fig. 23a), $f(\varepsilon) = (\rho_m/\rho_c)^{1/2}v(\varepsilon)$, $v(\varepsilon) = 1-\exp\left(-(1/2)\,m_T k_a\varepsilon\right)$, ρ_m is the maximum density of dislocations in the cell walls, ρ_c is the minimum density of dislocations in the bulk of cells [these two densities depend on the coefficients of multiplication of dislocations on the forest dislocations and of their immobilization on obstacles of nondeformation origin (impurities, precipitates, and so on)], k_a is the coefficient of annihilation of dislocations, and Λ is the size of the cells. Figure 23a shows the distribution of the dislocation density only in the direction x in the cellular structure, which in general has a three-dimensional character [212], because the cell walls in fcc crystals are located along characteristic (111)-type slip planes. Curves *1* and *2* in this figure demonstrate the dislocation densities for two degrees of deformation, $\varepsilon = 10\%$ and 50%, at $k_a = 5$, $\rho_m/\rho_c = 1.6\times10^3$, and $m_T = 3.05$.

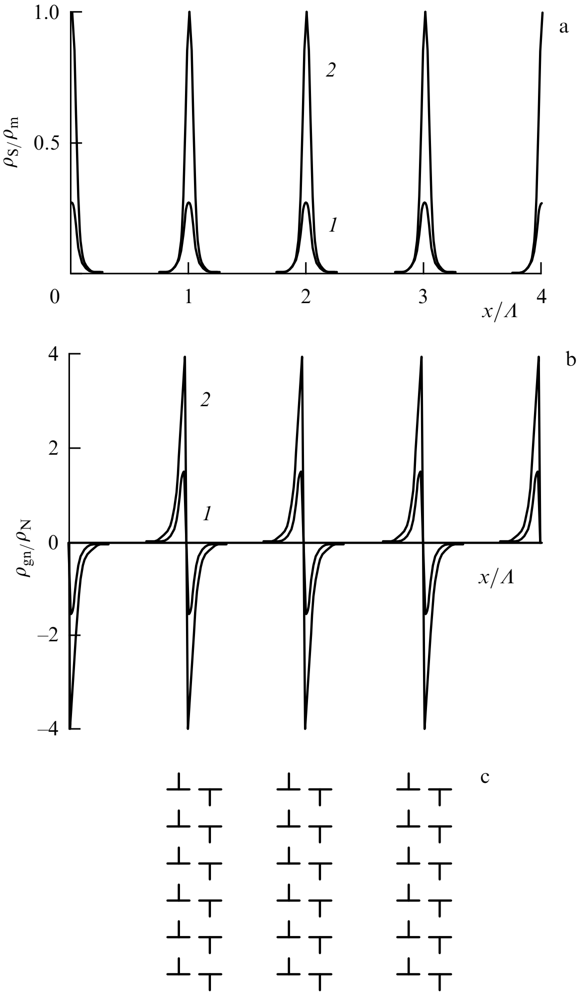

Figure 23. (a) Distribution of dislocations according to Eqns (37) and (38) in a cellular structure and (b) formation in it of paired walls at deformations of (*1*) 5% and (*2*) 50%; (c) a schematic of paired walls of GN dislocations.

The width of the walls of the dislocation cells $\Delta\Lambda$ is approximately equal to one-fourth of the cell dimension $\Lambda = 0.4-1$ μm [56, 209] (i.e., it is 100–250 nm), and the shear deformation reaches 20% or more. As a result, the cell walls are associated with large plastic deformation gradients and, correspondingly, with a high density of GN dislocations $\rho_{gn} = b^{-1}\,\partial\gamma_p/\partial x$. The shear deformation in a wall is determined by the Orowan formula $\gamma_p = b\rho_S(x,\varepsilon)\,\lambda_f$, where $\lambda_f(x,\varepsilon) = 1/\delta_f\,\rho_S^{1/2}(x,\varepsilon)$ is the length of the free path of dislocations through the forest of dislocations in the cell walls with, $\delta_f \approx 10^{-2}$. As a result, we have the following relation for the density of GN dislocations: $\rho_{gn}(x,\varepsilon) = \delta_f^{-1}\,\partial\rho_S^{1/2}(x,\varepsilon)/\partial x$. Substituting the density of statistical dislocations (37) in this relation, we obtain the distribution of the density of GN dislocations in the cell structure (Fig. 23b)

$$\rho_{\mathrm{gn}}(x,\varepsilon) = -\rho_{\mathrm{N}}\,\frac{\nu(\varepsilon)\left[f(\varepsilon)-1\right]\sin(2\pi x/\Lambda)}{\left[1+\left(f(\varepsilon)-1\right)\sin^2(\pi x/\Lambda)\right]^2}\,, \qquad (38)$$

where $\rho_{\mathrm{N}} = (\pi/\delta_{\mathrm{f}}\Lambda\rho_{\mathrm{m}}^{1/2})\,\rho_{\mathrm{m}} \approx 16\rho_{\mathrm{m}}$ at $\Lambda\rho_{\mathrm{m}}^{1/2} = 20$ [211].

It can be seen from Fig. 23b and from the key diagram given in Fig. 23c that at the position of the dislocation cell, the GN dislocations form two dislocation walls of finite width with a high density of dislocations in them, $\rho_{\mathrm{gn}} = (10-100)\,\rho_{\mathrm{S}} \approx 10^{15}-10^{16}$ m^{-2}. Such dense dislocation walls [196] arise at the initial stage of the formation of the blocked dislocation structure. In a transmission electron microscope, they look like dark, wide (compared to the cell walls) microbands, because these walls are associated with local lattice misorientation $\omega(x,\gamma) = \gamma_{\mathrm{p}}(x,\gamma) = \delta_{\mathrm{f}}^{-1} b\rho_{\mathrm{S}}^{1/2}(x,\gamma)$. At $\delta_{\mathrm{f}} = 10^{-2}$, $b = 0.25$ nm, and $\rho_{\mathrm{S}} = 10^{13}-10^{14}$ m^{-2}, we find that $\omega \approx 4^{\circ}-14^{\circ}$. At large plastic deformations, the high density of GN dislocations leads to the formation of additional fourth and fifth stages in the curves of strain hardening of fcc metals [219, 220].

As follows from the analysis of experimental data [209–212], the formation of blocked and cellular dislocation structures is related to processes of spatial self-organization of dislocations [56, 109], in particular, in the case under consideration, with the self-organization of GN dislocations. This is confirmed by the fact that just as in the case of cellular structures, the parameters of the blocked structure (size of blocks Λ [211, 212], width of their walls $\Delta\Lambda$ [209], angle of the block misorientation ω [210–212]) obey the similarity principle, i.e., change as the density of dislocations increases in accordance with the scaling laws $\Delta\Lambda \sim \Lambda \sim \rho^{-1/2}$ and $\omega \sim \rho^{1/2}$, preserving a constant ratio of these parameters.

For flow stresses at large plastic deformations, when a blocked structure is formed, the laws $\tau \sim \rho^{1/2} \sim \Lambda^{-1}$ are satisfied [211, 212], as in the case of a cellular structure. The $\tau \sim \Lambda^{-1}$ dependence indicates that in spite of the large angle of lattice misorientation, the block boundaries are disordered and nonequilibrium, i.e., consist, as in the cellular structure, of discrete dislocations, although predominantly of the same sign. After annealing at moderate temperatures and weak primary recrystallization, the boundaries become equilibrium, and the dependence of the flow stresses on the size d of the arising micrograins obeys the HP relation $\tau \sim d^{-1/2}$ [40, 221].

4. Conclusions

(1) It follows from the results of the investigations of the effect of grain size in the range 2–1000 nm (Section 2) on the strength and deformation properties of metallic materials that this effect can be both positive and negative. The positive effect occurs because the grain refinement substantially (by an order of magnitude) increases the resistance of the material to plastic deformation; the negative effect is related to a decrease in the resistance of the NC material to deformation localization (neck formation), which leads to a plastic rupture of the nanocrystalline sample at the early stage of deformation. These opposite tendencies are a consequence of the general regularity concerning the genetic interconnection between the strength and the reserve of plasticity under uniaxial compression of various materials [112–115].

Another characteristic feature of plastic deformation of nanocrystalline materials is the crossover (at the grain sizes less than 10–20 nm) from the grain-boundary strengthening (in accordance with the HP relation) of the nanomaterial to the mechanism of its grain-boundary softening related to the diffusional absorption and annihilation of dislocations in nanograin boundaries. The softening occurs at conventional temperatures, which strongly reduces the nanomaterial strength. But this circumstance also has a positive aspect, because it creates a technological base for high-strain-rate and low-temperature superplastic deformation of these materials.

The methods of improving the plastic properties of NC materials, such as the production of bimodal nanomicrograined and nanotwinned submicrograined structures, allow improving these properties (in the sense of increasing the uniform deformation prior to neck formation) without a substantial loss of strength. In connection with nanotwinned submicrograined structures, we note that the experiments revealed one unexpected circumstance: they showed that the boundaries of nanotwins, while absorbing and emitting lattice dislocations, lose their coherence and acquire the property inherent of nanograin boundaries — the ability to serve as sinks for dislocations.

An important aspect of plastic deformation of crystalline materials is the formation of GN dislocations due to the existence of large plastic deformation gradients on microscale and nanoscale levels in the boundaries of dislocation cells. At large plastic deformations (produced, for instance, using the method of equal-channel angular pressing), the generation and self-organization of GN dislocations leads to the formation of a blocked dislocation structure in the material, which results in the fragmentation of the material into strongly misoriented crystalline blocks (fragments) 100–200 nm in size, which increases the strength of the material compared to its initial state by an order of magnitude.

(2) As regards the strength of single-crystal samples in the form of thin films, micropillars, and microwires (whiskers) with transverse dimensions in the micro- and nanoranges, the experimental data presented in Section 3 unambiguously indicate that their strength grows as the crystals become thinner and perfection grows (the density of surface defects and dislocation sources decreases). The strength reaches the theoretical shear strength in the absence of defects. One specific feature of the mechanism of plastic deformation of nano- and microcrystals is that it is mainly controlled by two kinetic processes: the emission of dislocations from surface and subsurface dislocation sources and the escape of dislocations from the crystal through the surface. Both these processes substantially, but differently, depend on the transverse section of crystals. The detection of dislocation sources and their evolution in the process of deformation should be the subject of further investigations. The use of methods of molecular dynamics and dynamics of discrete dislocations, which have widely been used for studying the mechanism of the effect of the size factor on the strength and specific features of deformation of nanosized crystals, have allowed revealing the fine details of this influence, such as the generation of single-pole dislocation sources with critical lengths depending on the transverse dimension of a crystal.

(3) The analysis of the mechanism of the evolution of the strength and plasticity of NC metals and micro-and nanosized crystals performed in this review on the basis of the equations of dislocation kinetics permitted us to system-

atically, in a wide range of scales and in terms of a unified theoretical approach, investigate the effect of the size factor on the average density of dislocations and its variation depending on the degree of deformation in these materials. The equations derived take a number of circumstances characteristic of the plastic deformation of nanosized structures into account, such as the predominant role of nanograin boundaries and of the surface of nanocrystals — sources of, sinks for, and barriers to dislocations.

The use of a dislocation-kinetics analysis permitted us to quantitatively check, refine, and theoretically substantiate such features of deformation of nanosized crystals as the mechanisms of dislocation starvation and exhaustion of strain hardening. The refinements concern the effect of strain hardening on the initial (zeroth) stage of deformation of nanosized crystals, the stage of activation of dislocation sources. The existence of strain hardening at this stage follows from the dislocation-kinetics analysis of experimental data made in the review. This is confirmed by the data obtained in [222].

An advantage of the dislocation-kinetics approach, compared to other methods of the analysis of the mechanical behavior of crystalline materials, is the possibility of including some elementary kinetic processes on the microscopic level (generation of dislocations from dislocation sources, disappearance of dislocation at a sink, multiplication and annihilation of dislocations) in the kinetic equations for the evolution of the average density of dislocations in the material, depending on the deformation or the time, with various structural factors, such as size effects considered in this study, taken into account. A disadvantage of this approach is that it ignores statistical aspects of the phenomena. This circumstance should be taken into account when comparing the theory with the experiment, which correspond to each other within the spread of experimental data.

(4) In this review, in accordance with the task posed, we restricted ourselves to the analysis of studies in which the NC materials — nanocrystals and microcrystals — were subjected to only simple mechanical actions, namely, uniaxial tension, compression, or bending. In the literature, studies exist in which the nanomaterials and nanocrystals are deformed under more complex conditions, such as mechanical fatigue [223], impact loading [224], creep [2], and instability of sizes of nanograins at enhanced temperatures [225]. Because the strength and plastic properties of nanomaterials are determined by dislocations in all these cases, the dislocation-kinetics approach can likewise be applied to the analysis of their mechanical behavior under the above conditions. The results of its application to an analysis of superplastic deformation of micro- and nanomaterials can be found in [4, 40]. In [226], results of the dislocation-kinetics analysis of the effect of grain sizes on the impact toughness are given. It follows from these results that the fracture toughness decreases after the grains reach some small critical size, which was confirmed in experiment [227]. In [228], the dislocation-kinetics approach was used for an analysis of critical conditions of the formation of a cellular dislocation structure in metals under severe conditions of neutron irradiation. Other above-mentioned cases of the behavior of nanomaterials and alloys under complex conditions of loading should become the subject of further investigations in the framework of this approach.

References

1. Gleiter H *Prog. Mater. Sci.* **33** 223 (1989)
2. Sherby O D, Wadsworth J *Prog. Mater. Sci.* **33** 169 (1989)
3. Chokshi A H et al. *Scripta Metallurg.* **23** 1679 (1989)
4. Malygin G A *Fiz. Tverd. Tela* **37** 2281 (1995) [*Phys. Solid State* **37** 1248 (1995)]
5. Masumura R A, Hazzledine P M, Pande C S *Acta Mater.* **46** 4527 (1998)
6. Conrad H, Narayan J *Scripta Mater.* **42** 1025 (2000)
7. Valiev R Z, Islamgaliev R K, Alexandrov I V *Prog. Mater. Sci.* **45** 103 (2000)
8. Rybin V V *Bol'shie Plasticheskie Deformatsii i Razrushenie Metallov* (Large Plastic Deformations and Fracture of Metals) (Moscow: Metallurgiya, 1986)
9. Zhilyaev A P, Langdon T G *Prog. Mater. Sci.* **53** 893 (2008)
10. Abrosimova G E et al. *Fiz. Tverd. Tela* **49** 983 (2007) [*Phys. Solid State* **49** 1034 (2007)]
11. Lee M H et al. *Scripta Mater.* **58** 651 (2008)
12. Glezer A M, Manaenkov S E, Permyakova I E *Izv. Ross. Akad. Nauk, Ser. Fiz.* **71** 1745 (2007) [*Bull. Russ. Acad. Sci. Phys.* **71** 1702 (2007)]
13. Brenner S S *J. Appl. Phys.* **27** 1484 (1956)
14. Brenner S S *J. Appl. Phys.* **28** 1023 (1957)
15. Nadgornyi E M et al. *Usp. Fiz. Nauk* **67** 625 (1959) [*Sov. Phys. Usp.* **2** 282 (1959)]
16. Uchic M D et al. *Science* **305** 986 (2004)
17. Greer J R, Nix W D *Appl. Phys. A* **80** 1625 (2005)
18. Greer J R, Oliver W C, Nix W D *Acta. Mater.* **53** 1821 (2005)
19. Haque M A, Saif M T A *Sensors Actuators A* **97 – 98** 239 (2002)
20. Fleck N A et al. *Acta Metallurg. Mater.* **42** 475 (1994)
21. Stölken J S, Evans A G *Acta Mater.* **46** 5109 (1998)
22. Evans A G, Hutchinson J W *Acta. Mater.* **57** 1675 (2009)
23. Nix W D, Gao H *J. Mech. Phys. Solids* **46** 411 (1998)
24. Suresh S, Nieh T-G, Choi B W *Scripta Mater.* **41** 951 (1999)
25. Golovin Yu I *Fiz. Tverd. Tela* **5** 2113 (2008) [*Phys. Solid State* **50** 2205 (2008)]
26. Funakubo H (Ed.) *Shape Memory Alloys* (New York: Gordon and Breach, 1984)
27. Likhachev V A, Kuz'min S L, Kamentseva Z P *Effekt Pamyati Formy* (Shape Memort Effect) (Leningrad: Izd. LGU, 1987)
28. Khachin V N, Pushin V G, Kondrat'ev V V *Nikelid Titana: Struktura i Svoistva* (Titanium Nickelide: Structure and Properties) (Moscow: Nauka, 1992)
29. Malygin G A *Usp. Fiz. Nauk* **171** 187 (2001) [*Phys. Usp.* **44** 173 (2001)]
30. Vasil'ev A N et al. *Usp. Fiz. Nauk* **173** 577 (2003) [*Phys. Usp.* **46** 559 (2003)]
31. Kohl M *Shape Memory Microactuators* (Berlin: Springer, 2004)
32. San Juan J, Nó M L, Schuh C A *Adv. Mater.* **20** 272 (2008)
33. Malygin G A *Fiz. Tverd. Tela* **50** 1480 (2008) [*Phys. Solid State* **50** 1538 (2008)]
34. Yang H-S, Bhadeshia H K D H *Scripta Mater.* **60** 493 (2009)
35. Frick C P, Orso S, Arzt E *Acta Mater.* **55** 3845 (2007)
36. Frick C P et al. *Scripta Mater.* **59** 7 (2008)
37. Chen Y, Schuh C A *Acta Mater.* **59** 537 (2011)
38. Malygin G A *Zh. Tekh. Fiz.* **79** (12) 60 (2009) [*Tech. Phys.* **54** 1782 (2009)]
39. Meyers M A, Mishra A, Benson D J *Prog. Mater. Sci.* **51** 427 (2006)
40. Malygin G A *Fiz. Tverd. Tela* **49** 961 (2007) [*Phys. Solid State* **49** 1013 (2007)]
41. Dao M et al. *Acta Mater.* **55** 4041 (2007)
42. Armstrong R W, in *Mechanical Properties of Nanocrystalline Materials* (Ed. J C M Li) (Hackensack, NJ: World Sci. Publ., 2009) Ch. 3
43. Andrievski R A, Glezer A M *Usp. Fiz. Nauk* **179** 337 (2009) [*Phys. Usp.* **52** 315 (2009)]
44. Uchic M D, Shade P A, Dimiduk D M *Annu. Rev. Mater. Res.* **39** 361 (2009)
45. Dehm G *Prog. Mater. Sci.* **54** 664 (2009)
46. *Scripta Mater.* **48** (2) (2003)
47. Van Swygenhoven H, Farkas D, Caro A *Phys. Rev. B* **62** 831 (2000)

48. Hasnaoui A, Derlet P M, Van Swygenhoven H *Acta Mater.* **52** 2251 (2004)
49. Wolf D et al. *Acta Mater.* **53** 1 (2005)
50. Kuksin A Yu, Stegailov V V, Yanilkin A V *Fiz. Tverd. Tela* **50** 1984 (2008) [*Phys. Solid State* **50** 2069 (2008)]
51. Zhou C, Biner S B, LeSar R *Acta Mater.* **58** 1565 (2010)
52. Espinosa H D et al. *Proc. Natl. Acad. Sci. USA* **102** 16933 (2005)
53. Rao S I et al. *Acta Mater.* **56** 3245 (2008)
54. Fertig R S, Baker S P *Prog. Mater. Sci.* **54** 874 (2009)
55. Motz C et al. *Acta Mater.* **57** 1744 (2009)
56. Malygin G A *Usp. Fiz. Nauk* **169** 979 (1999) [*Phys. Usp.* **42** 887 (1999)]
57. Shi J, Zikry M A *Mater. Sci. Eng. A* **520** 121 (2009)
58. Malygin G A *Fiz. Tverd. Tela* **52** 48 (2010) [*Phys. Solid State* **52** 49 (2010)]
59. Gryaznov V G et al. *J. Mater. Sci.* **28** 4359 (1993)
60. Gutkin M Yu, Ovid'ko I A *Fizicheskaya Mekhanika Deformiruemykh Nanostruktur* (Physical Mechanics of Deformable Structures) Vol. 1 *Nanokristallicheskie Materialy* (Nanocrystalline Materials) (St. Petersburg: Yanus, 2003)
61. Kolesnikova A L, Ovid'ko I A, Romanov A E *Pis'ma Zh. Tekh. Fiz.* **33** (15) 26 (2007) [*Tech. Phys. Lett.* **33** 641 (2007)]
62. Gutkin M Yu, Ovid'ko I A *Fiz. Tverd. Tela* **50** 630 (2008) [*Phys. Solid State* **50** 655 (2008)]
63. Pozdnyakov V A, Glezer A M *Fiz. Tverd. Tela* **44** 705 (2002) [*Phys. Solid State* **44** 732 (2002)]
64. Glezer A M *Izv. Ross. Akad. Nauk, Ser. Fiz.* **67** 810 (2003) [*Bull. Russ. Acad. Sci. Phys.* **67** 893 (2003)]
65. Park H S, Gall K, Zimmerman J A *Phys. Rev. Lett.* **95** 255504 (2005)
66. Malygin G A *Fiz. Tverd. Tela* **43** 1286 (2001) [*Phys. Solid State* **43** 1339 (2001)]
67. Inagaki H *Z. Metallk.* **83** 97 (1992); *Z. Metallk.* **83** 304 (1992)
68. Pinsook U, Ackland G J *Phys. Rev. B* **62** 5427 (2000)
69. Howe J M, Pond R C, Hirth J P *Prog. Mater. Sci.* **54** 792 (2009)
70. Tu J et al. *J. Mater. Sci.* **29** 1662 (1994)
71. Glezer A M, Blinova E N, Pozdnyakov V A *Izv. Ross. Akad. Nauk, Ser. Fiz.* **66** 1263 (2002)
72. Giga A et al. *Scripta Mater.* **55** 143 (2006)
73. Wang Y M, Ma E *Appl. Phys. Lett.* **83** 3165 (2003)
74. Wei Q et al. *Mater. Sci. Eng. A* **381** 71 (2004)
75. Cheng S et al. *Acta Mater.* **53** 1521 (2005)
76. Asaro R J, Suresh S *Acta Mater.* **53** 3369 (2005)
77. Chen J, Lu L, Lu K *Scripta Mater.* **54** 1913 (2006)
78. Wang Y M, Hamza A V, Ma E *Acta Mater.* **54** 2715 (2006)
79. Malygin G A *Fiz. Tverd. Tela* **49** 2161 (2007) [*Phys. Solid State* **49** 2266 (2007)]
80. Detor A J, Schuh C A *Acta Mater.* **55** 371 (2007); Trelewicz J R, Schuh C A *Acta Mater.* **55** 5948 (2007)
81. Wei Q et al. *Appl. Phys. Lett.* **81** 1240 (2002)
82. Jia D, Ramesh K T, Ma E *Acta Mater.* **51** 3495 (2003)
83. Malygin G A *Fiz. Tverd. Tela* **51** 1709 (2009) [*Phys. Solid State* **51** 1814 (2009)]
84. Nachum S et al. *Mater. Sci. Eng. A* **527** 5065 (2010)
85. Wang Y et al. *Nature* **419** 912 (2002)
86. Gil Sevillano J, Aldazabal J *Scripta Mater.* **51** 795 (2004)
87. Pozdnyakov V A *Izv. Ross. Akad. Nauk, Ser. Fiz.* **71** 1751 (2007) [*Bull. Russ. Acad. Sci. Phys.* **71** 1708 (2007)]
88. Malygin G A *Fiz. Tverd. Tela* **50** 990 (2008) [*Phys. Solid State* **50** 1056 (2008)]
89. Phaniraj M P, Prasad M J N V, Chokshi A H *Mater. Sci. Eng. A* **463** 231 (2007)
90. Malygin G A *Fiz. Tverd. Tela* **50** 1013 (2008) [*Phys. Solid State* **50** 1032 (2008)]
91. Sasaki T T, Ohkubo T, Hono K *Acta Mater.* **57** 3529 (2009)
92. Srinivasarao B et al. *Acta Mater.* **57** 3277 (2009)
93. Lu L et al. *Science* **304** 422 (2004)
94. Ma E et al. *Appl. Phys. Lett.* **85** 4932 (2004)
95. Lu L et al. *Acta Mater.* **53** 2169 (2005)
96. Chen X H, Lu L *Scripta Mater.* **57** 133 (2007)
97. Lu L et al. *Science* **323** 607 (2009)
98. Lu K, Lu L, Suresh S *Science* **324** 349 (2009)
99. Lu L et al. *Scripta Mater.* **60** 1062 (2009)
100. Lu L et al. *Acta Mater.* **57** 4933 (2009)
101. Wang G et al. *Mater. Sci. Eng. A* **527** 4270 (2010)
102. Li J C M, Chou Y T *Metallurg. Trans.* **1** 1145 (1970)
103. Youssef K M et al. *Appl. Phys. Lett.* **87** 091904 (2005)
104. Wu X-L, Ma E *Appl. Phys. Lett.* **88** 231911 (2006)
105. Bitzek E et al. *Acta Mater.* **56** 4846 (2008)
106. Dorn J E, Rajnak S *Trans. Metal. Soc. AIME* **230** 1052 (1964)
107. Malygin G A *Fiz. Met. Metalloved.* **58** 360 (1984)
108. Cross M C, Hohenberg P C *Rev. Mod. Phys.* **65** 851 (1993)
109. Malygin G A *Fiz. Tverd. Tela* **37** 3 (1995) [*Phys. Solid State* **37** 1 (1995)]
110. Han Z et al. *Appl. Phys. Lett.* **93** 231912 (2008)
111. Chen M *Annu. Rev. Mater. Res.* **38** 445 (2008)
112. Malygin G A *Fiz. Tverd. Tela* **47** 236 (2005) [*Phys. Solid State* **47** 246 (2005)]
113. Malygin G A *Fiz. Tverd. Tela* **47** 632 (2005) [*Phys. Solid State* **47** 656 (2005)]
114. Malygin G A *Fiz. Tverd. Tela* **47** 870 (2005) [*Phys. Solid State* **47** 896 (2005)]
115. Malygin G A *Fiz. Tverd. Tela* **53** 341 (2011) [*Phys. Solid State* **53** 363 (2011)]
116. Shen Y F et al. *Scripta Mater.* **52** 989 (2005)
117. Zhang Y, Tao N R, Lu K *Scripta Mater.* **60** 211 (2009)
118. Li Y S, Tao N R, Lu K *Acta Mater.* **56** 230 (2008)
119. Sanders P G, Eastman J A, Weertman J R *Acta Mater.* **45** 4019 (1997)
120. Wang H L, Wang Z B, Lu K *Acta Mater.* **59** 1818 (2011)
121. Zhu T et al. *Proc. Natl. Acad. Sci. USA* **104** 3031 (2007)
122. Jin Z-H et al. *Acta Mater.* **56** 1126 (2008)
123. Lian J, Baudelet B *Mater. Sci. Eng.* **84** 157 (1986)
124. Suzuki H, Ikeda S, Takeuchi S *J. Phys. Soc. Jpn.* **11** 382 (1956)
125. Yoshida K, Gotoh Y, Yamamoto M *J. Phys. Soc. Jpn.* **24** 1099 (1968)
126. Diehl J *Z. Metallkd.* **47** 331 (1956)
127. Malygin G A *Fiz. Tverd. Tela* **35** 1698 (1993) [*Phys. Solid State* **35** 1470 (1993)]
128. Kramer I R, Podlaseck S *Acta Metallurg.* **11** 70 (1963)
129. Kramer I R, Demer L J *Prog. Mater. Sci.* **9** 133 (1961)
130. Rosi F D *Acta Metallurg.* **5** 348 (1957)
131. Nakada Y, Chalmers B *Trans. AIME* **230** 1339 (1961)
132. Kramer I R, Demer L J *Trans. AIME* **221** 780 (1961)
133. Latanision R M, Staehle R W *Acta Metallurg.* **17** 307 (1969)
134. Malygin G A *Fiz. Tverd. Tela* **35** 1328 (1993) [*Phys. Solid State* **35** 855 (1993)]
135. Berner R, Kronmüller H "Plastische Verformung von Einkristallen", in *Moderne Probleme der Metallphysik* Vol. 1 (Ed. A Seeger) (Berlin: Springer-Verlag, 1965) [Translated into Russian: *Plasticheskaya Deformatsiya Monokristallov* (Plastic Deformation of Single Crystals) (Moscow: Mir, 1969)]
136. Uchic M D, Dimiduk D M *Mater. Sci. Eng. A* **400–401** 268 (2005)
137. Coulombier M et al. *Scripta Mater.* **62** 742 (2010)
138. Dimiduk D M, Uchic M D, Parthasarathy T A *Acta Mater.* **53** 4065 (2005)
139. Frick C P et al. *Mater. Sci. Eng. A* **489** 319 (2008)
140. Norfleet D M et al. *Acta Mater.* **56** 2988 (2008)
141. Shan Z W et al. *Nature Mater.* **7** 115 (2007)
142. Greer J R, Nix W D *Phys. Rev. B* **73** 245410 (2006)
143. Volkert C A et al. *Appl. Phys. Lett.* **89** 061920 (2006)
144. Volkert C A, Lilleodden E T *Philos. Mag.* **86** 5567 (2006)
145. Lee D et al. *Scripta Mater.* **56** 437 (2007)
146. Dou R, Derby B *Scripta Mater.* **59** 151 (2008)
147. Dou R, Derby B *Scripta Mater.* **61** 524 (2009)
148. Kim J-Y, Greer J R *Acta Mater.* **57** 5245 (2009)
149. Motz C, Schöberl T, Pippan R *Acta Mater.* **53** 4269 (2005)
150. Kiener D et al. *Adv. Eng. Mater.* **8** 1119 (2006)
151. Kiener D et al. *Acta Mater.* **56** 580 (2008)
152. Zhao Y H et al. *Scripta Mater.* **59** 627 (2008)
153. Gruber P A et al. *Acta Mater.* **56** 2318 (2008)
154. Ng K S, Ngan A H W *Scripta Mater.* **59** 796 (2008)
155. Ng K S, Ngan A H W *Acta Mater.* **56** 1712 (2008)
156. Lederer M et al. *Mater. Sci. Eng. A* **527** 590 (2010)
157. Buzzi S et al. *Philos. Mag.* **89** 869 (2009)
158. Dou R, Xu B, Derby B *Scripta Mater.* **63** 308 (2010)
159. Bei H et al. *Scripta Mater.* **57** 397 (2007)

160. Bei H et al. *Acta Mater.* **56** 4762 (2008)
161. Kim J-Y, Greer J R *Appl. Phys. Lett.* **93** 101916 (2008)
162. Greer J R, Weinberger C R, Cai W *Mater. Sci. Eng. A* **493** 21 (2008)
163. Lowry M B et al. *Acta Mater.* **58** 5160 (2010)
164. Kim J-Y, Jang D, Greer J R *Acta Mater.* **58** 2355 (2010)
165. Kim J-Y, Jang D, Greer J R *Scripta Mater.* **61** 300 (2009)
166. Schneider A S et al. *Mater. Sci. Eng. A* **508** 241 (2009)
167. Schneider A S et al. *Phys. Rev. Lett.* **103** 105501 (2009)
168. Han S M et al. *Scripta Mater.* **63** 1153 (2010)
169. Nadgorny E M, Dimiduk D M, Uchic M D *J. Mater. Res.* **23** 2829 (2008)
170. Dimiduk D M et al. *Philos. Mag.* **90** 3621 (2010)
171. Oh S H et al. *Nature Mater.* **8** 95 (2009)
172. Kiener D, Minor A M *Acta Mater.* **59** 1328 (2011)
173. Senger J et al. *Scripta Mater.* **58** 587 (2008)
174. El-Awady J A et al. *Phys. Rev. B* **80** 104104 (2009)
175. Zhou C, Biner S, LeSar R *Scripta Mater.* **63** 1096 (2010)
176. Segall D E, Li C, Xu G *Philos. Mag.* **86** 5083 (2006)
177. Zhu T et al. *Phys. Rev. Lett.* **100** 025502 (2008)
178. Li C, Xu G *Philos. Mag.* **86** 2957 (2006)
179. Parthasarathy T A et al. *Scripta Mater.* **56** 313 (2007)
180. Nowak J D et al. *Scripta Mater.* **62** 819 (2010)
181. Ogata S et al. *Phys. Rev. B* **70** 104104 (2004)
182. Von Blanckenhagen B, Gumbsch P, Arzt E *Philos. Mag. Lett.* **83** 1 (2003)
183. Begau C et al. *Acta Mater.* **59** 934 (2011)
184. Lee S-W, Han S M, Nix W D *Acta Mater.* **57** 4404 (2009)
185. Zhou C, Biner S B, LeSar R *Acta Mater.* **58** 1565 (2010)
186. Malygin G A *Fiz. Tverd. Tela* **29** 2067 (1987) [*Sov. Phys. Solid State* **29** 1189 (1987)]
187. Yoshida K, Goto Y, Yamamoto M *J. Phys. Soc. Jpn.* **21** 825 (1966)
188. Gotoh Y *J. Appl. Phys.* **44** 1382 (1973)
189. Jang D, Greer J R *Scripta Mater.* **64** 77 (2011)
190. Ashby M F *Philos. Mag.* **21** 399 (1970)
191. Mughrabi H *Mater. Sci. Eng. A* **387 – 389** 209 (2004)
192. Motz C, Schöberl T, Pippan R *Acta Mater.* **53** 4269 (2005)
193. Ehrler B et al. *Philos. Mag.* **88** 3043 (2008)
194. Xiang Y, Vlassak J J *Acta Mater.* **54** 5449 (2006)
195. Gao H, Huang Y *Scripta Mater.* **48** 113 (2003)
196. Hughes D A, Hansen N, Bammann D J *Scripta Mater.* **48** 147 (2003)
197. Urusovskaya A A, Thyagarajan R *Phys. Status Solidi B* **10** 349 (1965)
198. Higashida K, Takamura J, Narita N *Mater. Sci. Eng.* **81** 239 (1986)
199. Karduck P et al., in *Textures of Materials: Proc. of the Fifth Intern. Conf. on Textures of Materials, March 28 – 31, 1978, Aachen, Germany* Vol. 1 (Eds G Gottstein, K Lücke) (Berlin: Springer-Verlag, 1978) p. 377
200. Malygin G A *Fiz. Tverd. Tela* **32** 1102 (1990) [*Sov. Phys. Solid State* **32** 561 (1990)]
201. Nye J E *Acta Metallurg.* **1** 153 (1953)
202. Wei C T, Beck P A *J. Appl. Phys.* **27** 1508 (1956)
203. Malygin G A *Fiz. Tverd. Tela* **44** 1249 (2002) [*Phys. Solid State* **44** 1305 (2002)]
204. Malygin G A *Fiz. Tverd. Tela* **34** 2882 (1992) [*Sov. Phys. Solid State* **34** 1543 (1992)]
205. Gektina I V et al. *Metallofizika* **9** (2) 33 (1987)
206. Washburn J, Parker E R *J. Metals* **4** 1076 (1952)
207. Gubicza J et al. *Mater. Sci. Eng. A* **387 – 389** 55 (2004)
208. Hughes D A et al. *Acta Mater.* **45** 105 (1997)
209. Malygin G A *Fiz. Tverd. Tela* **44** 1979 (2002) [*Phys. Solid State* **44** 2072 (2002)]
210. Malygin G A *Fiz. Tverd. Tela* **46** 1968 (2004) [*Phys. Solid State* **46** 2035 (2004)]
211. Malygin G A *Fiz. Tverd. Tela* **48** 651 (2006) [*Phys. Solid State* **48** 693 (2006)]
212. Malygin G A, in *Proc. The Second Int. Symp. on Physics and Mechanics of Large Plastic Strains, St. Petersburg, Russia, June 4 – 9, 2007, "Prometey"*; *Vopr. Materialoved.* (4(52)) 260 (2007)
213. Nabarro F R N, Basinski Z S, Holt D B *Adv. Phys.* **13** 193 (1964) [Translated into Russian: *Plastichnost' Chistykh Monokristallov* (Plasticity of Pure Single Crystals) (Moscow: Metallurgiya, 1967)]
214. Kawasaki Y *J. Phys. Soc. Jpn.* **36** 142 (1974)
215. Liu Q, Jensen D J, Hansen N *Acta Mater.* **46** 5819 (1998)
216. Hughes D A, Hansen N *Acta Mater.* **48** 2985 (2000)
217. Malygin G A *Fiz. Tverd. Tela* **31** (1) 175 (1989) [*Sov. Phys. Solid State* **31** 96 (1989)]
218. Malygin G A *Fiz. Tverd. Tela* **31** (7) 43 (1989) [*Sov. Phys. Solid State* **31** 1123 (1989)]
219. Zehetbauer M, Seumer V *Acta Metallurg. Mater.* **41** 577 (1993)
220. Malygin G A *Fiz. Tverd. Tela* **43** 1832 (2001) [*Phys. Solid State* **43** 1909 (2001)]
221. Tsuji N et al. *Scripta Mater.* **47** 893 (2002)
222. Maaß R et al. *Acta Mater.* **57** 5996 (2009)
223. Vinogradov A Yu et al. *Mater. Sci. Eng. A* **318** 163 (2001)
224. Botvina L R et al. *Ross. Nanotekhnol.* **2** (1–2) 106 (2007)
225. Morris D G, Muñoz-Morris M A *Acta Mater.* **50** 4047 (2002)
226. Malygin G A *Fiz. Tverd. Tela* **48** 1622 (2006) [*Phys. Solid State* **48** 1716 (2006)]
227. Li S X, Cui G R *J. Appl. Phys.* **101** 083525 (2007)
228. Malygin G A *Fiz. Tverd. Tela* **48** 455 (2006) [*Phys. Solid State* **48** 484 (2006)]